ANNALS OF GEOPHYSICS, 2026; doi:10.4401/ag-9584
OPEN ACCESS

Ionospheric responses to the May 2024 geomagnetic storm over the East-Southeast Asia and Australia

Dung Nguyen Thanh[1], Minh Le Huy[*,1], Susumu Saito[2], Christine Amory-Mazaudier[3], Roland Fleury[4], Thanh Le Truong[1], Thang Nguyen Chien[1], Hong Pham Thi Thu[1], Tam Dao[5], Thanh Nguyen Ha[1], Mai Nguyen Thi[1], Michi Nishioka[6], Septi Perwitasari[6]

(1) Institute of Earth Sciences, Vietnam Academy of Science and Technology, Hanoi, Vietnam
(2) Electronic Navigation Research Institute, MPAT, Tokyo, Japan
(3) Sorbonne Université, UPMC University, Paris, France
(4) Institut Mines-Telecom Atlantique, LAB-STICC, UMR 6285, Brest, France
(5) RMIT University, SPACE Research Centre, School of Science, Melbourne, Australia
(6) National Institute of Information and Communications Technology, Tokyo, Japan

Article history: received April 17, 2026; accepted October 24, 2026

Abstract

This study utilizes GPS-derived total electron content (TEC), critical frequency (foF_2) from ionosondes, TEC from Swarm satellite measurements, the [O]/[N_2] ratio from TIMED/GUVI, and the vertical electron density profiles from COSMIC to examine the ionospheric response over the East-Southeast Asia and Australian sector during the May 2024 magnetic storm, the strongest since November 2003. The storm began at 17:05 UT on May 10, marked by a Sudden Storm Commencement (SSC) with an amplitude of approximately 74 nT in the SYM-H index, which rapidly declined to about −518 nT by 02:14 UT on May 11. GNSS receiver chains were used to study the morphology of the equatorial ionization anomaly (EIA) during the entire storm period. During the main phase, a negative ionospheric storm effect was observed, as indicated by the decrease in foF_2 at the PHUT and BACL stations and TEC at both of hemispheres. The decrease in foF_2 and TEC is believed to be caused by the impact of the prompt penetration electric field (PPEF). A complex evolution of the EIA morphology was observed during the recovery phase. During the recovery phase on May 11, hmF_2 exhibited repeated uplifts over Southeast Asia in response to fluctuating PPEF associated with successive southward-to-northward and northward-to-southward reversals of the interplanetary magnetic field (IMF) B_z before 15:00 UT. On May 11, the EIA structure showed degradation, with a double-peak morphology in both hemispheres associated with strong PPEF fluctuations. The EIA crests shifted equatorward, and an enhancement/reduction of foF_2 at the equator/near EIA crest region in the Northern Hemisphere was observed, which is associated with PPEF, equatorward meridional winds and changes in [O]/[N_2] ratio. The effect of the ionospheric disturbance dynamo was identified from magnetic data at PHUT and GUAM observatories. The disappearance of the northern EIA crest observed on May 12 might have resulted from the combined influence of factors such as the ionospheric disturbance dynamo effect, meridional winds (the equatorward meridional and transequatorial meridional winds), and the decrease in the [O]/[N_2] density ratio. Hemispheric asymmetry of the EIA was observed during the first two days of the recovery phase (May 11-12). On May 13, an increase in the amplitude of the southern crest (14 TECU) was observed compared to May 12; the northern crest reappeared, and both crests showed a tendency to shift polewards.

Keywords: Mother's Day Magnetic Storm; Equatorial Ionization Anomaly; East-Southeast Asia-Australian Sector; Prompt Penetration Electric Field; Disturbance Dynamo Electric Field

1. Introduction

The modern views suggest that powerful solar storms are accompanied by UV and EUV flux enhancements, X-ray flares, solar cosmic ray flux increases, and shock waves driven by coronal mass ejections or high-speed solar wind components, cause disturbances commonly termed the geospace storm (GSS). GSS is composed by interacting storms in the magnetosphere, atmosphere, ionosphere, lithosphere, and in the geophysical fields (magnetic, electric, barometric pressure, and thermal ones). GSS significantly affect the correct functioning of space- and ground-based telecommunications systems. GSS impact the precision of radio navigation, radar, radio astronomy, radio soundings of Earth from space and of geospace from Earth, as well as human well-being and human health (Chernogor, 2025a,b). The effects of GSS are often associated with changes in the geomagnetic field and ionosphere (magnetic storm, ionospheric storm), and therefore these changes are of great concern.

The high-latitude ionosphere is directly linked to variations in the interplanetary magnetic field through open magnetic field lines, resulting in strong reactions such as alterations in thermospheric circulation and plasma convection in those regions (Fuller-Rowell et al., 1994; Kelley et al., 2003). In contrast, low-latitude and equatorial ionospheric regions are not directly affected by interplanetary magnetic activity. However, they are disturbed through the electrodynamic coupling between the high and low-latitude ionosphere regions. This coupling occurs through mechanisms: (1) Intense auroral particle precipitation ionizes neutral gas, increases the conductivity and the auroral ionospheric electric current. Joule heating energy dissipated by ionospheric electric currents in the ionosphere/thermosphere is the major energy source during storms (Lu et al., 1995). Heating of the thermosphere drives equatorward wind surges and causes an upwelling at high latitudes, which carries heavier neutrals upward and increases the mean molecular mass (Rishbeth et al., 1987; Burns et al., 1991; Fuller-Rowell et al., 1994; Lin et al., 2005). The region of increased molecular mass, also known as the region of composition disturbance, can be transported equatorward by the storm-time and background neutral wind fields (Prölss, 1995; Fuller-Rowell et al., 1998). The component perturbation is characterized by the density ratio $[O]/[N_2]$ as is commonly seen in magnetic storm studies. (2) The PPEF occurs over a short period (hours or less) (Nishida, 1968; Vasyliunas, 1970; Fejer et al., 1979, 1990; Kikuchi et al., 2000; Tsurutani et al., 2008; Balan et al., 2018). (3) The ionospheric disturbance dynamo electric field (DDEF) occurs over longer timescales (Blanc and Richmond, 1980; Fejer and Scherliess, 1995; Fuller-Rowell et al., 2002; Richmond et al., 2003; Mannucci et al., 2005). (4) Neutral winds during storms influence the transport of plasma parallel to magnetic field lines and the diffusion process (Lin et al., 2005; Ambili et al., 2025). During magnetic storms, the ionospheric response in the equatorial and low-latitude regions is primarily reflected in changes in the EIA. The combination of the above physical mechanisms can explain the observed suppression of EIA, the shift in EIA crest location, and the negative/positive storm effects at equatorial/low-latitudes region.

On May 8, 2024, the Space Weather Prediction Center (SWPC) issued a warning about an imminent severe space weather event after following the detection of multiple solar flares heading toward Earth by both ground- and space-based telescopes. On May 10, 2024, a significant influx of solar plasma impacted Earth, marking it as the most severe storm in the past 20 years. The solar storm was classified as “extreme” by the U.S. National Oceanic and Atmospheric Administration (www.swpc.noaa.gov/news/severe-and-extreme-g4-g5-geomagnetic-storms-likely-12-may-2024), resulting in the aurora borealis being visible across numerous countries. The geomagnetic storm pushed auroral displays to appear at lower magnetic latitudes (e.g., Ghosh, 2024; Greshko, 2024). According to NOAA’s Space Weather Prediction Center, the magnetic storm caused power grid irregularities, loss of high-frequency communications, and GPS disruptions. This storm was named the Mother’s Day storm (Spogli et al., 2024).

It is well known that magnetic storms significantly impact the ionosphere through various physical mechanisms, and the Mother’s Day storm presents an opportunity to enhance our understanding of ionospheric dynamics. To date, there have been many published studies on the ionospheric responses of this super storm over different regions. Studies have been reported in the Mediterranean sector (Spogli et al., 2024) and the American-Atlantic longitude sector (Aa et al., 2024; Tulasi Ram et al., 2024). However, these studies were conducted in longitude sectors with local time conditions different from those of the East-Southeast Asia and Australia sector, and therefore the ionospheric responses to the geomagnetic storm may exhibit certain differences among regions. Several studies (Ambili et al., 2025; Jain et al., 2025; Ashok et al., 2025; Krisman et al., 2025) have provided detailed investigations of ionospheric responses over the Indian equatorial and low-latitude region during the May 2024 geomagnetic storm. However, observations from the Southern Hemisphere were not included in these studies.

Meanwhile, detailed investigations of ionospheric disturbances associated with the May 2024 superstorm have also been carried out over the East Asia-Australia sector. Huang et al. (2025) demonstrated that abnormal ionospheric

changes were attributed to meridional wind disturbances associated with AGWs and recurrent penetration electric fields corresponding to larger B_z southward excursions and disturbance dynamo. Guo et al. (2024) observed a negative ionospheric storm, characterized by a significant and prolonged decrease in electron density over the entire region of China just after the SSC on May 10 at 18:00 UT. This ionospheric storm persisted during the main phase and the beginning of the recovery phase. During the recovery phase on the daytime of May 12, a strong and long-lasting negative storm effect remained in the eastern part of China except for a few local medium-scale increases. Meanwhile, a positive storm effect followed by a weak negative storm possible due to strengthening of the northward wind, appeared in the western part. The east-west asymmetry in the response found in the studied region is thought to be a general pattern for the supper magnetic storms that possibly caused by an arch shape structure of enhanced $\Sigma[O]/[N_2]$. Sun et al. (2024) showed that the ionospheric fluctuations occurring following the storm onset created multiple oscillating crests embedded in the TEC diurnal variation. Along the same latitude, the fluctuations were nearly synchronized over longitude span up to 35°, which contained two major origins over magnetic equator and high latitudes respectively. The former could be due to the multiple penetrations of the eastward electric field associated with southward excursion of IMF B_z. The latter originated from highlatitudes were manifested as large-scale Travelling Ionospheric Disturbances (TIDs) propagating equatorward. Changes at low latitudes are more visible and complicated, because they are affected by disruptions coming from both the equator and high-latitude regions. The fluctuations at low latitude were most significant and complex, which were under the influence by the disturbances sourced from both equatorial and high-latitude regions. Over different longitude sectors, the finescale ionospheric behavior may exhibit different features possibly depending on local time. However, these studies have not investigated in depth the north-south asymmetry during the storm period. Zhang et al. (2024) also reported negative storm effects in the Northern Hemisphere and positive storm effects in the Southern Hemisphere, which may be related to changes in the $[O]/[N_2]$ ratio associated with the global circulation. However, in this study, we report that the negative/positive storm effects in the Northern/Southern Hemisphere persisted into May 12, extending the duration reported by Zhang et al. (2024), showing that the interhemispheric asymmetric response persisted for a longer duration than previously reported.

We present, for the first time, observations of the Mother's Day storm recorded by Vietnamese observatories: two ionosondes (PHUT and BACL), one geomagnetic observatory (PHUT) and fourteen GNSS stations (BACL, CLAN, DANH, DLAT, HUUL, HOAB, HUS2, LSON, PHUT, QOAI, QHOA, SOCS, TANY and TLAC) distributed across Vietnam, spanning from the equatorial region to low latitudes; the detailed structure of the EIA can be better characterized. The objective of this study is to examine the variations in the equatorial/low-latitude ionosphere and their interactions with the mid- and high-latitude regions during all phases of the storm. The paper utilizes a range of data sources available (GNSS, $[O]/[N_2]$, vertical sounding and magnetic, data from Swarm and COSMIC-2/FORMOSAT-7) to highlight the ionospheric response over the East-Southeast Asia and Australian sector to the Mother's Day storm from May 08 to 22, 2024. From there, we hope that the results of this paper can contribute to a better understanding of the impact of space weather events on the ionosphere, spanning from mid-latitudes to the equator. Section 2 describes the data and methods, section 3 presents the results, sections 4 and 5 include a discussion and conclusions.

2. Data sets and Data processing

2.1 Solar wind data

In this study, we examine the solar wind parameters: Vx, the component of the solar wind speed following the Sun-Earth axis, which estimates the magnitude of the solar wind disturbances, and B_z, the component of the interplanetary magnetic field (IMF), directed southward at the main phase of the magnetic storms.

These parameters are obtained from the ACE Science Center http://izw1.caltech.edu/ACE/ASC/level2/lvl2DATA_SWEPAM.html.

2.2 Magnetic indices

The SYM-H index available at World Data Center for Geomagnetism, Kyoto, Japan (https://wdc.kugi.kyoto-u.ac.jp/dst_realtime/index.html) and Kp geomagnetic activity index at (https://kp.gfz-potsdam.de/en/) is also used to estimate the intensity of the geomagnetic storm.

2.3 GNSS data and data processing

The primary dataset used in this study consists of data obtained from continuous GNSS stations over the East-Southeast Asia and Australian sector. Figure 1 gives the location of the GNSS stations and Table 1 lists their names and geographic coordinates.

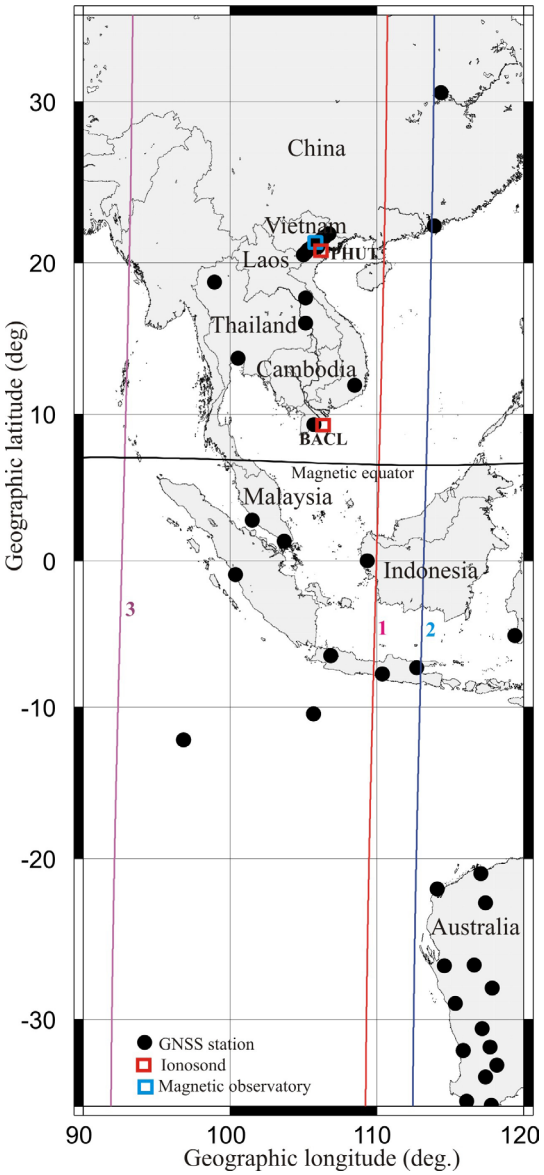


Figure 1. The distribution of used GNSS receivers, ionosondes and magnetic observatory in the East-Southeast Asia and Australian sector. Solid color lines represent the ground track projection of the Swarm B passages at about 03:33 UT (1-red) on May 10, about 03:15 UT (2-blue) on May 11, about 04:32 UT (3-magenta) on May 12, 2024. The magnetic equator is located at about 7°N latitude.

The carrier-phase measurements between the GPS satellites and receivers were used to calculate the TEC along the signal path (i.e., the slant TEC, sTEC) following the methodology described by Le Huy et al. (2016) and Carter et al. (2023). The possible jumps in the sTEC values estimated from the carrier-phase measurements due to cycle slips were eliminated by comparing them against the sTECp estimated from the pseudo-range measurements that were smoothed by a fourth-degree polynomial approximation. A change in the carrier-phase sTEC of more than 5 TECU was taken to indicate an instrumental data jump/spike; in such instances, the change in the carrier-phase sTEC was substituted by the change in the smoothed sTECp. The sTEC was then compared with the Center of Orbit

Determination in Europe Global model to determine the total delay of device (including biases), using elevation angles above 30° to remove multipath effects. The total delay of device is calculated for each satellite-receiver pair at each observation time, and the daily total delay of device is taken as the average. Finally, the resulting sTEC was converted to the vertical total electron content (VTEC) observed at the pierce point of the ionosphere by using a single-layer model (Klobuchar, 1986) and an assumed altitude of 400 km (Zhao et al., 2009).

Table 1. List of GNSS, ionospheric, and magnetic stations.

No.	Station	Geographic coordinate		No.	Station	Geographic coordinate	
		Long. (deg)	Lat. (deg)			Long. (deg)	Lat. (deg)
1	8KLN	118.15806	−32.67029	23	KARR	117.09720	−20.98142
2	ALBY	117.81019	−34.95022	24	KELN	117.70264	−31.62231
3	ANMG	101.50660	2.78465	25	LSON	106.74906	21.85260
4	BACL	105.71102	9.29903	26	NCLF	116.12327	−34.70837
5	BAKO	106.84891	−6.49106	27	NKAY	105.15000	17.72000
6	BURA	117.174645	−30.52551	28	NTUS	103.67996	1.34580
7	CMUM	98.93238	18.76088	29	MEDO	114.60956	−26.75738
8	CLAN	106.44731	21.67466	30	MRO1	116.63749	−26.69663
9	CMAK	119.40802	−5.13480	31	MTMA	117.84310	−28.11531
10	COCO	96.83398	−12.18834	32	PERT	115.88526	−31.80196
11	CPDG	100.36311	−0.95398	33	PHUT	105.95872	21.02938
12	CPON	109.32904	−0.00362	34	QOAI	105.49226	20.95633
13	CUSV	100.53392	13.73591	35	QHOA	104.99143	20.52457
14	CSBY	112.72436	−7.33433	36	SOCS	105.91935	21.29166
15	DANH	105.78528	21.16494	37	TANY	106.07433	21.40704
16	DLAT	108.41420	15.79284	38	TLAC	105.18232	20.69587
17	EXMT	114.11338	−21.96067	39	TOAY	105.15000	16.07000
18	HKSL	113.92798	22.37200	40	TOMP	117.40031	−22.84645
19	HUUL	106.28930	21.55973	41	XMIS	105.68849	−10.44997
20	HOAB	105.32750	20.84219	42	YARR	115.34698	−29.04658
21	HUS2	105.84638	21.00450	43	WAGN	117.41010	−33.33306
22	JOG2	110.37238	−7.76381	44	WUHN	114.35727	30.53165

2.4 Ionosondes data and data processing: computation of $\vec{E} \wedge \vec{B}$ drift

The two ionosondes at Phu Thuy (PHUT) (21.03°N, 105.96°E, dip: 15.95°N) and Bac Lieu (BACL) (9.28°N, 105.73°E, dip: 3.31°N) are presented on Fig. 1 and listed in the Table 1. The ionosonde data of BACL station is available on the website https://wdc.nict.go.jp/Ionosphere/archive/ionog_viewer_fmcw_ms/ and free accessible. The ionosonde data of PHUT station which are in the database of the Institute of Earth Sciences (https://ies.vast.vn), can be obtained by sending a request to vp@ies.vast.vn. The real height of the F2-layer peak density-hmF_2 is obtained by real-height inversion of ionograms using POLAN (Titheridge, 1985).

The vertical drift velocity $\vec{E} \wedge \vec{B}$ of the layer F is estimated by the formula (Oyekola et al., 2007):

$$V_z(t) = \frac{hmF_2(t + \Delta t) - hmF_2(t - \Delta t)}{2\Delta t}$$

The daily hour values hmF_2 have been used, so $\Delta t = 1$h.

2.5 Magnetic data and D_{dyn} calculation

The Earth's magnetic field data at Phu Thuy (PHUT) geomagnetic observatory are used to compute D_{dyn}. For comparison, D_{dyn} is compute from the data of GUAM observatory (144.87°E, 13.59°N).

During a magnetic storm, the H component of Earth's magnetic field observed at a magnetic observatory can be decomposed as the following surperposition:

$$H = H_0 + S_q^H + D_{mag} + D_{iono} \tag{1}$$

where H_0 is the 4-hour midnight average value of component H, S_q^H is the average diurnal variation of the 5 quietest days of the month in the H component, D_{mag} is the disturbance caused by the turbulent current system in the magnetosphere, mainly the ring current, is estimated by the SYM-H index. During a geomagnetic storm, the equatorial ring current plays a crucial role within the magnetosphere, indicated by SYM-H index, so the magnetic disturbances caused by current systems in the ionosphere D_{iono} is the disturbance of the current-systems in the ionosphere:

$$D_{iono} = H - H_0 - S_q^H - (SYM - H) * \cos\phi \tag{2}$$

where ϕ is magnetic latitude of the geomagnetic observatory. Magnetic disturbances related to the disturbance dynamo effect D_{dyn} could be estimated by using the wavelet semblance analysis methodology (Younas et al., 2021). Semblance analysis (Cooper and Cowan, 2008) compares the local phase relation between two datasets as function of time and wavelength. This can be done by performing a cross wavelet transform ($CWT_{1,2}$) of two time series (Torrence and Compo, 1998), defined as:

$$CWT_{1,2} = CWT_1 \cdot CWT_2^* \tag{3}$$

where * denotes the complex conjugate. The cross-wavelet transform (3) is a complex quantity having an amplitude $\alpha = |CWT_{1,2}|$ and local phase $\theta = \tan^{-1}\left(\frac{\mathrm{Im}(CWT_{1,2})}{\mathrm{Re}(CWT_{1,2})}\right)$, where Im and Re denote the imaginary and real parts, respectively. The semblance is evaluated as (Cooper and Cowan, 2008):

$$semblance = \cos^n(\theta) \tag{4}$$

where n is positive odd integer (n = 1). In equatorial low latitude region D_{dyn} contrasts with respect to S_q (Le Huy and Mazaudier, 2005), so it can be obtained by:

$$D_{dyn} = \alpha\left[anticorr\left\{semblance\left(S_q^H, D_{iono}\right)\right\}\right] \tag{5}$$

The Eq. (5) means that the contributions having a positive correlation between S_q and D_{iono} are neglected. Duration of D_{dyn} is estimated by considering the time interval from the start of disturbance till the normalized D_{dyn} reduces to a threshold value 0.3 (Younas et al., 2021).

2.6 [O]/[N_2] data

In additional, the [O]/[N_2] ratio obtained from the TIMED mission (https://spdf.gsfc.nasa.gov/pub/data/timed/guvi/) is employed. The primary process generating O^+ plasma in the F layer is the photoionization of molecular Oxygen, while the O^+ loss process includes reactions with atomic species such as N_2 and O_2. Consequently, the density of O^+ is likely to fluctuate with changes in the [O]/[N_2] ratio. Therefore, this data can provide insights into how the thermosphere composition influences the variability of ionospheric plasma density during storms (Spogli et al., 2024).

2.7 Data from the Swarm and COSMIC/FORMOSAT-7 satellite missions

TEC obtained from Swarm satellite measurements are utilized to compare with TEC values from GNSS measurements. The ESA's Swarm satellite mission (Friis-Christensen et al., 2008) comprises a constellation of three satellites, named Alpha (A), Bravo (B), and Charlie (C), which operate in quasi-Sun-synchronous near-polar low-Earth orbits at varying altitudes. In Mother Day's storm, Swarm A and C orbit at an altitude of approximately 480 km above the Earth's surface, while Swarm B operates at a higher altitude of about 510 km. The ground track projections of Swarm B passages over the study region on May 10-12, 2024 are presented in Fig. 1.

Electron density profiles from COSMIC-2 (Constellation Observing System for Meteorology, Ionosphere, and Climate-2) derived using the Abel inversion technique applied to radio occultation measurements, are sourced from the COSMIC Data Analysis and Archive Center (CDAAC).

3. Results

3.1 Global context of the geomagnetic storm

Figures 2a-e respectively illustrate the Vx component of the solar wind, the B_z component of the interplanetary magnetic field (IMF), SYM-H index, Kp index, and H-component of the geomagnetic field observed at PHUT observatory from the May 8 to 22, 2024 in Universal Time. The vertical lines in Fig. 2c indicate the SSC and the beginning of recovery phase of the storm.

Figure 2a shows that the Vx component increased abruptly from approximately 450 km/s to around 700 km/s at 16:36 UT on May 10, reaching a maximum at about 1000 km/s at 00:54 UT on May 12, it then declined gradually and returned to about 400 km/s on May 17-22, 2024. Figure 2b shows that the IMF B_z component underwent several northward-southward reversals on May 10-11, 2024. On May 10, a notable southward turning occurred at 16:36 UT (from 1.55 nT to –8.01 nT), accompanied by an increase in the solar wind velocity Vx, reaching a minimum of –44.9 nT at 17:36 UT. Subsequently, B_z underwent several north-south reversals, indicating complex fluctuations until around 15:00 UT on May 11, after which it gradually turned northward and returned to quiet-time levels, with small variations around zero on May 12. The ionosphere response to the variations of the IMF B_z component during May 10-13 will be discussed in the following.

The SYM-H index (Fig. 2c) indicates that the magnetic storm started at 17:05 UT on May 10, 2024 with an SSC amplitude of 74 nT. The SYM-H index then rapidly declines during the main phase (MP) and reaches a minimum of –518 nT at around 02:14 UT on May 11, 2024. The difference of about 29 minutes between the storm onset at Vx and B_z and the storm onset at the SYMH index is the transmission time of the storm's influence from the Lagrange point (about 1.5 million km from the Earth) to the Earth's surface. After 02:14 UT on May 11, 2024, the SYM-H index increases gradually in the recovery phase returning to pre-storm normal values by the end of May 22, 2024, making the end of the magnetic storm.

The Kp magnetic activity index (Fig. 2d) indicated extreme geomagnetic storm, with values between 8-9 from 18 UT on May 10 to 18 UT on May 11, 2024. On May 12, the maximum value of Kp was 6.3 (6^+); on May 13, 15 and 17, it was 6. On May 22, the activity returned to a quiet level and the maximum value of Kp was 1.6 (2^-).

Figure 2e illustrates the horizontal component variation of the magnetic field observed at PHUT observatory from May 8 to 22, 2024. The figure shows that the SSC recorded at PHUT at 17:07 UT on May 10, with an SSC amplitude of ~118 nT, then decreased rapidly to reach the minimum value of ~38585 nT at 10:17 UT on May 11. After hitting its minimum, the H component gradually increases to normal level on May 22. The decrease of the H component in the main phase of the storm was about 600 nT. The paper will further analyze and discuss the variation of the H component in the subsequent sections.

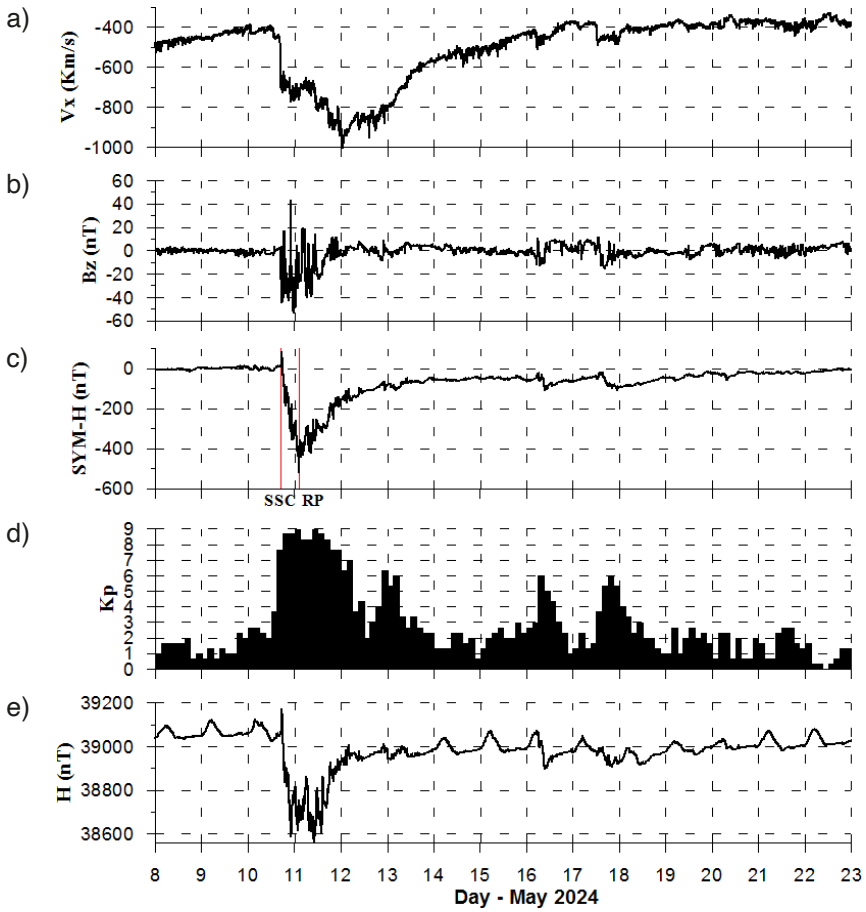


Figure 2. (a) Vx component of the solar wind, (b) B_z component of the interplanetary magnetic field, (c) SYM-H, (d) Kp index, (e) H-component observed at Phu Thuy observatory from May 08 to 22, 2024.

3.2 Variation of equatorial ionization anomaly crest during the magnetic storm

Figure 3 illustrates the TEC maps in the East-Southeast Asia and Australian sector using the stations in the longitude range of 96°-120°E from May 8 to 14, 2024. These maps were generated using the method of running average of overlapping windows, employing a window size of 1hx1° and sliding steps 0.75hx0.75° (Le Huy et al., 2014), and then gridded with the step 0.1hx0.1°. The equatorial ionization anomaly develops during the daytime; with the station network as shown in Fig. 1, the time-latitude TEC mapping techniques mentioned above can fully enable the determination of crest parameters with the necessary accuracy to study the temporal variation of the EIA crest parameters during magnetic storms in the studied region (Le Huy et al., 2016; Kalita et al., 2024; Choudhary et al., 2025). The horizontal red line underlies the magnetic equator (ME) at latitude 7°N according to the IGRF2020 model. The black vertical lines on the map represent the sudden onset and the beginning of recovery phase of the magnetic storm. The maps reveal a nearly symmetrical structure of the equatorial ionization anomaly (EIA) (Namba and Maeda, 1939; Appleton, 1946) around the magnetic equator, featuring a crest in the Northern Hemisphere at approximately 18°-20°N and a crest in the Southern Hemisphere at around 5°-7°S. The morphology of the equatorial ionization anomaly varies continuously from day to day throughout the storm period.

On May 11, the storm entered the recovery phase, the morphology of the EIA changed markedly compared to quiet days. Two EIA crests were observed to be still clearly visible, but with signs of degradation. On May 12, the morphological structure of the EIA exhibited a distinctly different pattern. While the northern EIA crest completely disappeared, the southern crest remained clearly pronounced. Another interesting feature observed in Fig. 3 is that the TEC in mid-latitude regions from approximately 20°S -39°S (geographic latitude, indicated by the red rectangle in Fig. 3) on May 12 increased compared to the quiet days.

The main phase lasted from 17:05 UT on May 10 to 02:14 UT on May 11, corresponding to local nighttime (00:05 LT on May 10) and morning hours (09:14 LT on May 11) in the study region. These local time conditions are associated

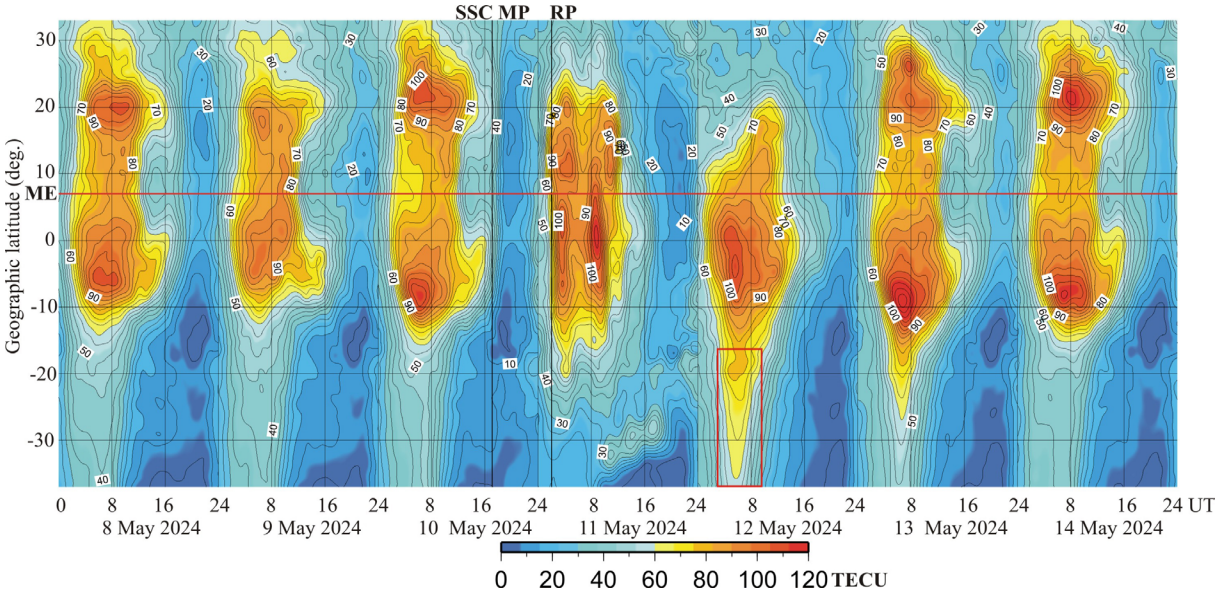


Figure 3. Temporal and latitudinal TEC maps from May 8 to 14, 2024. Contour interval: 5 TECU. SSC: Sudden Storm Commencement; MP: Main phase of the storm; RP: Beginning of the Recovery Phase of the storm. ME: magnetic equator.

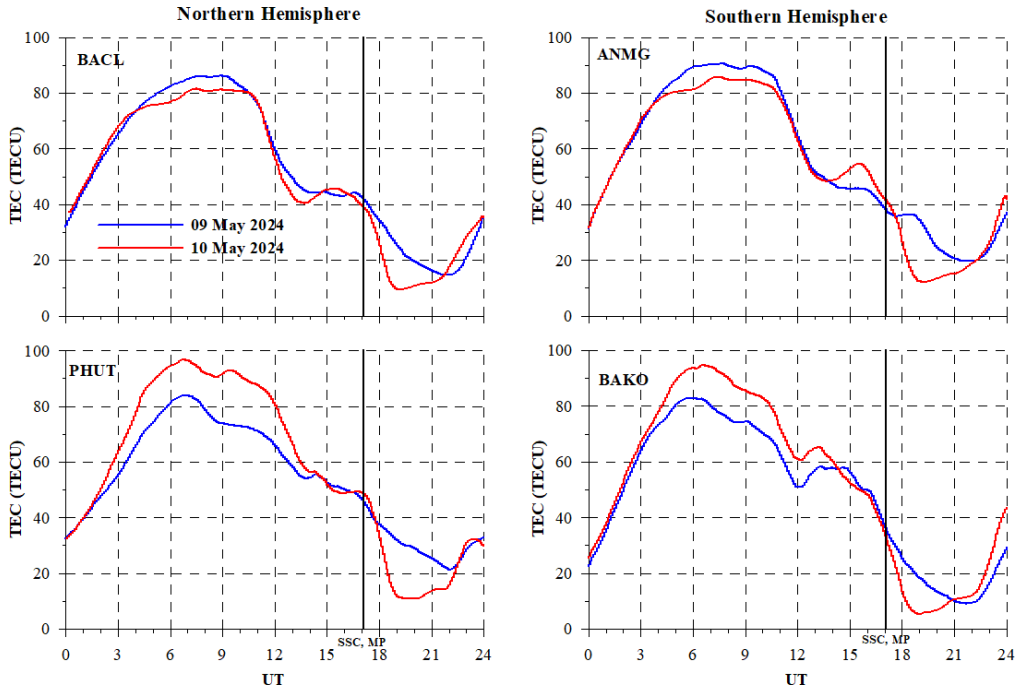


Figure 4. Daily TEC variation on May 9-10 at some stations in the studied region.

with a weakened or underdeveloped EIA. Therefore, it is difficult to identify any significant difference in the EIA structure from the TEC maps during this period compared with quiet-time conditions. However, the decline in TEC during the main phase can also be seen in the daily TEC variation at stations in both EIA crest and equatorial regions of both hemispheres (Fig. 4).

Figure 5 shows the temporal variation of the parameters: a) TEC maximum, b) appearance time (time when TEC reaches its maximum) and c) geographic latitude of the two crests (latitude of two maximum TEC points) from May 08 to 22, 2024. The corresponding parameters for the average TEC map of the 5 quietest days of May 2024 are shown by open rhombus. The TEC maximum at the average TEC map is close to the TEC maximum on May 9, the geographic latitudes of the crests are also near the latitudes of the northern and southern crests, and the appearance time falls within the variation range of appearance times of two crests. Figure 5 shows that the TEC amplitude of the southern crest is consistently higher than that of the northern one throughout the entire study period, because in this season, the fountain effect is deflected southward due to the magnetic dipole is tilted and the mean meridional wind is southward (Seba et al., 2018). However, the TEC amplitudes of both crests fluctuate at the same value of approximately 30 TECU. The occurrence time of the northern crest appears to oscillate more (~6 hours) than the occurrence time of the southern one (~4 hours). On May 10, the EIA crests appeared at around 13:30 LT at the daytime, before the onset of the geomagnetic storm. Therefore, the daytime EIA crests on this day were unaffected by the storm. On May 11, 2024, the first day of the recovery phase, the amplitude of the northern crest decreased compared to May 10, while the amplitude of the southern crest slightly increased. Notably, the occurrence time of the southern crest was about 5 hours later than that of the northern crest, and both crests tend to move toward the equator. On May 12, while the northern EIA crest disappeared, the amplitude of the southern crest remained comparable to that on May 10-11, and was even higher than on quiet days. The crest position shifted poleward compared to May 11, but still remained closer to the equator than during quiet days.

Another interesting feature observed in Fig. 5 is the enhanced TEC of the southern crest on May 13 compared to quiet days, at a time when the SYM-H index had nearly returned to its pre-storm level. The latitudinal ranges of both anomaly crests extended further poleward than on quiet days, especially for the northern EIA crest.

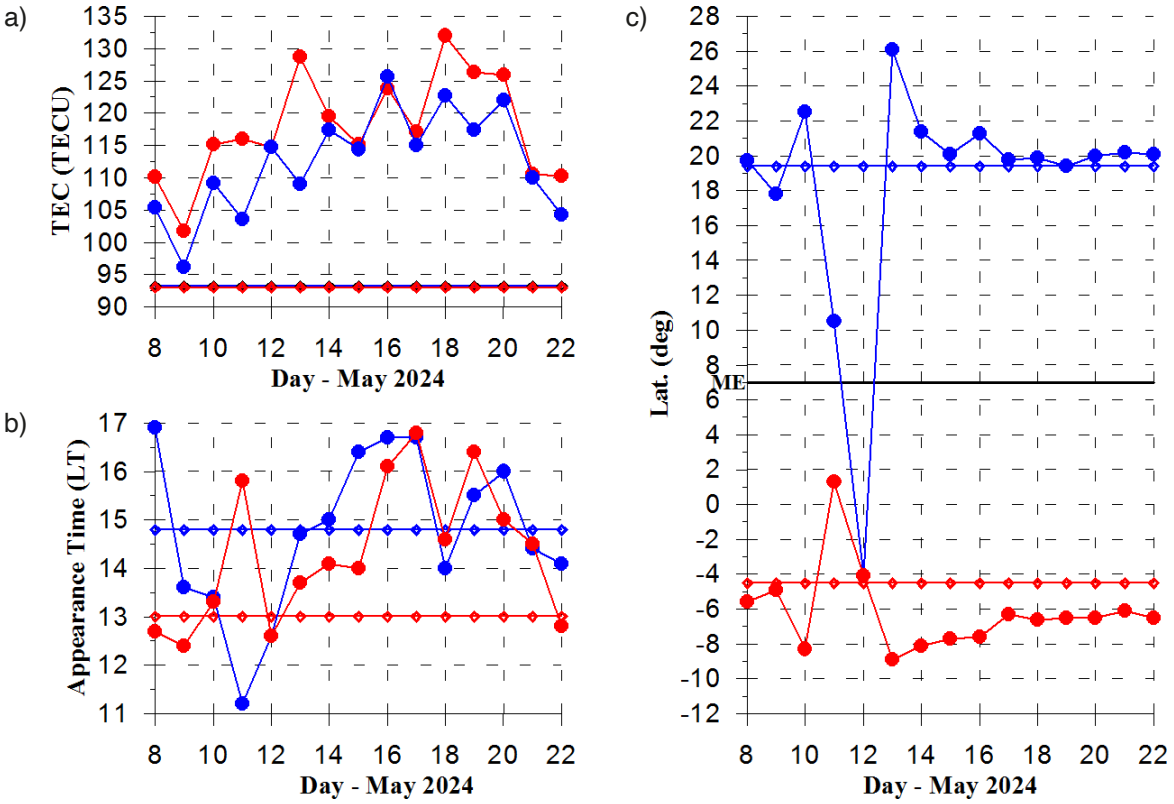


Figure 5. (a) Maximum TEC, (b) appearance time, and (c) latitude of the northern (solid blue cycle) and southern (solid red cycle) EIA crests from May 8 to 22, 2024. The corresponding parameters for the average TEC map of the 5 quietest days are shown by open rhombus.

3.3 Ionosonde measurements of the F2 layer at Phu Thuy and Bac Lieu

Figure 6 presents the parameters hmF_2 and foF_2 of the F2 layer at the low mid-latitude station PHUT (located near the EIA crest) and the equatorial station BACL (located in the EIA trough) and the IMF B_z component during may 10-13. Five geomagnetically quiet days in May 2024 (days 4, 9, 22, 25, 28) were selected as reference days, and their mean values were superimposed to estimate storm-induced variations. We observe that the variation of hmF_2

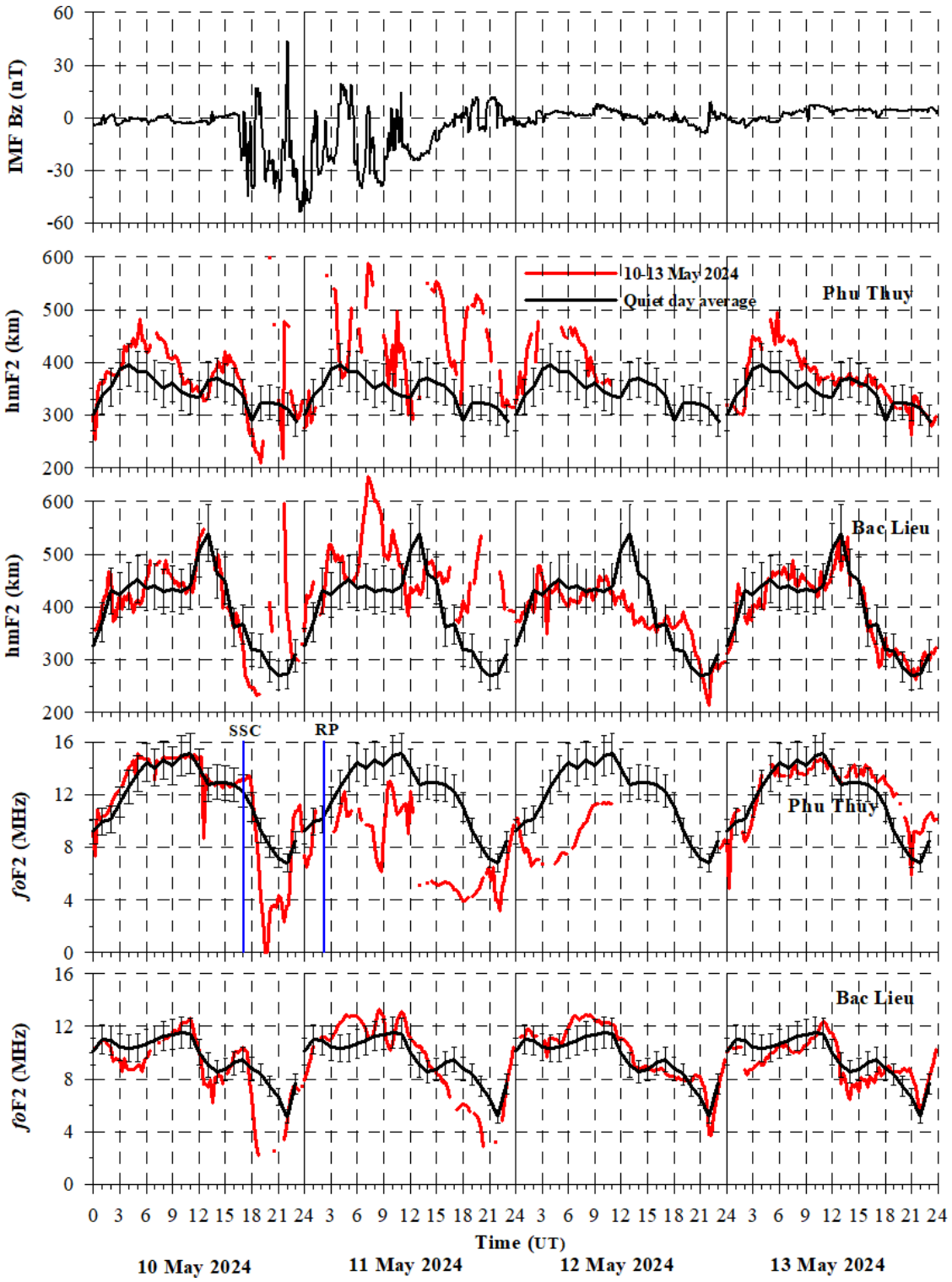


Figure 6. The variations of IMF B_z component and F2 layer parameters hmF_2 and foF_2 at PHUT and BACL from May 10 to 13, 2024. Unmarked data gaps are due to lack of data during these periods.

during the storm main phase on the night of May 10 and on the first day of the recovery phase (May 11) exhibits a different magnitude compared to its variation during the subsequent recovery days (May 12-13). Figure 7 presents a zoom-in view of this period from Fig. 6. Key events along the UT time axis are marked by vertical blue lines and numbered, allowing for a direct assessment of the magnetospheric and ionospheric conditions at those times. When the IMF B_z turned southward at around 16:40 UT (line 1), the hmF_2 height and foF_2 at both BACL and PHUT stations simultaneously decreased relative to the quiet-day values.

Subsequently, the IMF B_z turned northward and remained so for a short interval (line 2) from 21:52 to 22:16 UT (04:52-05:16 LT), corresponding to the local daytime period. The subsequent westward overshielding electric field opposed the upward vertical drift leading to a decrease in the F2-layer height at the magnetic equator. Consequently, the equatorial plasma fountain effect was weakened, and foF_2 at the equator decreased.

Thereafter, the IMF B_z turned southward at around 22:16 UT on May 10 and remained in this state until 03:59 UT on May 11 (line 3), persisting for a prolonged period. The hmF_2 at the equator exhibits fluctuations but remains higher than the quiet-day values. The foF_2 at the equator increase relative to the quiet-day values, whereas at the near EIA crest they decrease compared to the quiet-day values. During the interval 03:59-05:40 UT on May 11, within the recovery phase, the IMF B_z turned northward (line 4), the hmF_2 height and foF_2 at both the equator and the near EIA crest decreased.

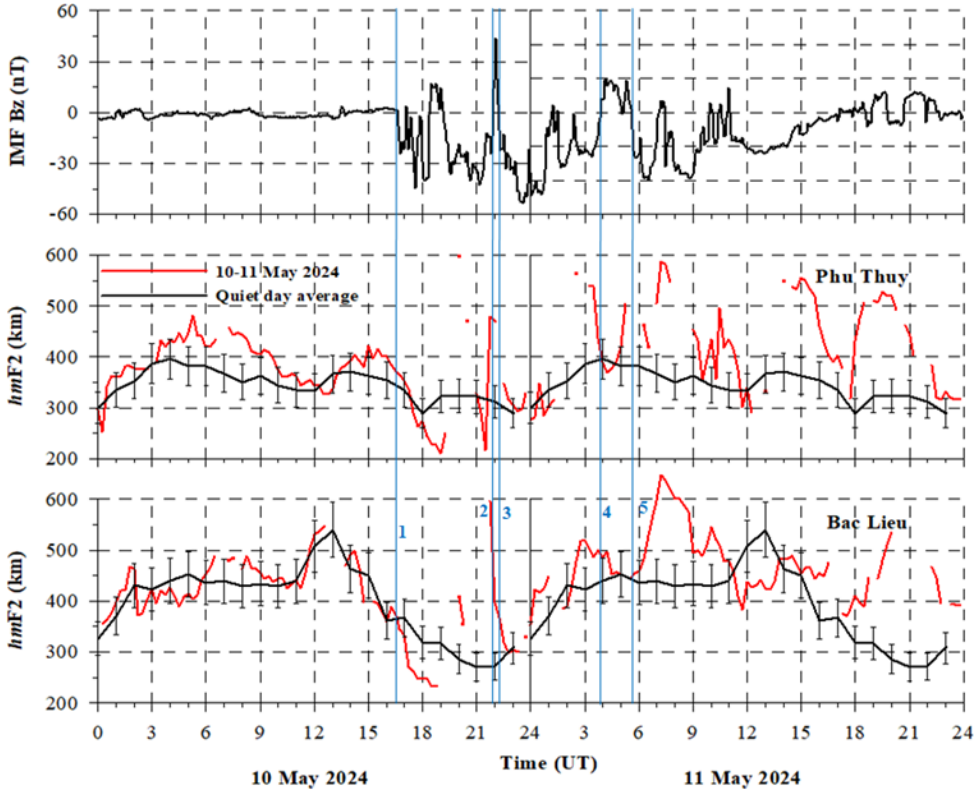


Figure 7. The variations of IMF B_z component and of hmF_2 in PHUT and BACL on May 10 and 11, 2024. Vertical lines 1-5 indicate the times when B_z changes direction from south to north or vice versa.

The IMF B_z then turned southward (line 5). During this interval, the hmF_2 height at the equator exhibited complex fluctuations and can be divided into several phases. During 06:00-11:00 UT, the hmF_2 at both BACL and PHUT increased significantly compared to the quiet-day values; however, foF_2 at the near EIA crest remained low, while at the equator they exhibited a slight increase relative to the quiet-day values. During 1 h 40 min period from 07:10-08:50 UT, the hmF_2 increased substantially to values well above typical daytime levels (exceeding 500 km). The foF_2 at BACL showed only a slight increase, whereas at PHUT it decreased markedly compared to the quiet-day values. During this interval, the ionograms at the equator show the presence of an F3 layer (at virtual height around 800-900 km) above the F2 layer of the ionosphere (Fig. 8).

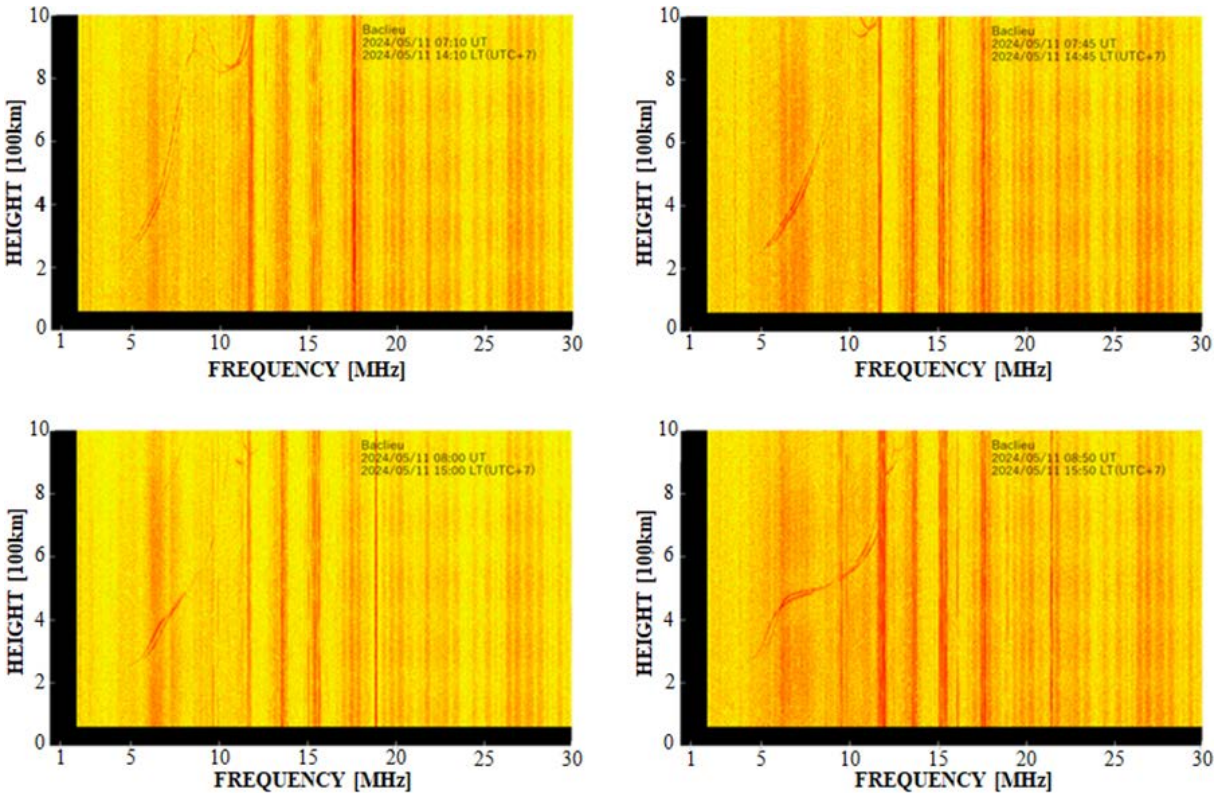


Figure 8. Ionograms show the presence of a F3 Layer on May 11, 2024 at a magnetic equator station (BACL).

On the second day of the recovery phase, May 12, hmF_2 height at the equator decreased compared to quiet-day conditions, whereas the height at low-mid latitudes showed little variation. The IMF B_z turned northward at around 15:00 UT on May 11 and subsequently fluctuated steadily around zero. The foF_2 at the equator exhibited a slight increase compared to quiet-day conditions, whereas near the anomaly crest, it decreased significantly relative to quiet days. These observations are also connected with the suppression of the northern EIA crest, as mentioned in the previous section. On May 13, hmF_2 and foF_2 at BACL and PHUT returned to levels comparable to quiet-day conditions. However, the TEC map observations presented earlier indicate that the ionospheric response on this day was rather interesting.

3.4 GUVI measurements of the ratio $[O]/[N_2]$

Figure 9a shows maps of the $[O]/[N_2]$ ratio derived from the Global Unltraviolet Imager (GUVI) onboard the Thermosphere Ionosphere Mesosphere Energetics and Dynamics (TIMED) satellite on May 10-13, 2024, with ratio values represented by different colors. Figure 9b shows the daily mean $[O]/[N_2]$ ratio obtained from TIMED/GUVI measurements over the same region covered by GNSS receivers and ionosondes in the Northern Hemisphere during May 8 to 22, 2024. The approximate location of the study region is indicated by the rectangle. In the Southern Hemisphere, $[O]/[N_2]$ ratio is observed only in part of the equatorial and low-latitude region (in magnetic latitude). On May 11, Fig. 9a shows that the region of low $[O]/[N_2]$ ratios had expanded equatorward to approximately 30°N over Asia, while regions of enhanced $[O]/[N_2]$ ratios were mainly confined to the equatorial regions of both hemispheres. The Fig. 9b reveals a significant drop in the $[O]/[N_2]$ ratio on May 11, which corresponds with a reduction in the amplitude of the northern EIA crest (as shown in Fig. 5) and a decrease in foF_2 in PHUT (as shown in Fig. 6). TIMED/GUVI observations on May 11 indicate that the hemispheric asymmetry of the $[O]/[N_2]$ ratio in the equatorial and low-latitude regions is broadly consistent with the asymmetry in EIA crest amplitude described in Section 3.1. On May 12, the average $[O]/[N_2]$ ratio over the Northern Hemisphere increased compared with May 11 but remained lower than its pre-storm level. However, the TIMED/GUVI images (Fig. 9a) show that the region of depleted $[O]/[N_2]$ ratios had penetrated equatorward to approximately 10°N over the East Asian sector. This suggests that the decrease in foF_2

near the northern EIA crest and the disappearance of the northern EIA crest were associated with the depletion of the [O]/[N_2] ratio. By May 13, the boundary of the low [O]/[N_2] region had retreated poleward to approximately 30°N. Due to the lack of [O]/[N_2] data in the Southern Hemisphere, we supplement observations from the Swarm and Cosmic satellites to facilitate discussion of the hemispheric asymmetry of the EIA, particularly on May 12 in the followings.

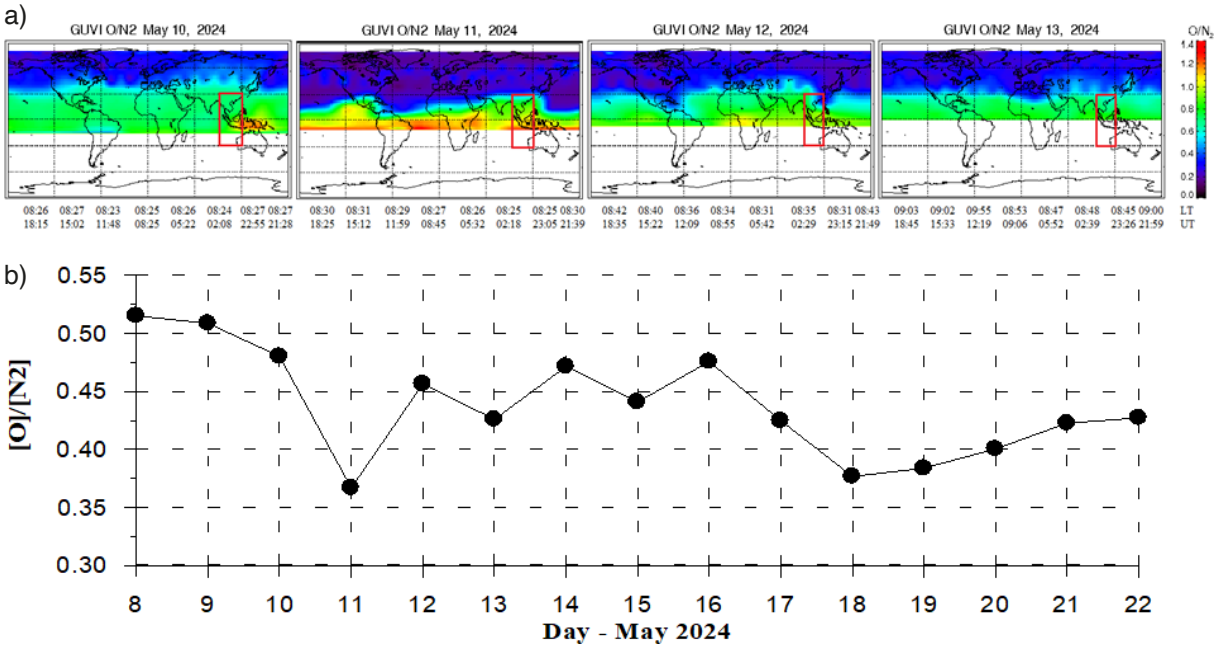


Figure 9. The TIMED/GUVI images [O]/[N_2] ratio on May 10-13, 2024 (a), and the daily mean [O]/[N_2] ratio obtained by TIMED/GUVI measurements over the East-Southeast Asia and Australian sector in the Northern Hemisphere from May 08 to 22, 2024 (b).

3.5 TEC from Swarm satellite measurements

Figure 10 illustrates the comparison of TEC obtained from GNSS and from Swarm B satellite measurements. The solid lines represent GNSS TEC profiles, while the dash-dash lines represent Swarm TEC profiles at about 03:33 UT on May 10 (red), about 03:15 UT on May 11 (blue) and about 04:31 UT on May 12 (purple). The black lines represent the TEC profiles on the average TEC map of the 5 quietest days of May 2024 at three corresponding moments. At the aforementioned times, the EIA is at its most active stage of the day; the average TEC profiles exhibit a distinct 2 crest structure on either side of the magnetic equator, with the southern crest larger than the northern one, as also seen in Fig. 3; at 04:31 UT, these two crests are almost symmetrical across the magnetic equator. On May 10 at 03:33 UT, prior to the onset of the magnetic storm, the GNSS TEC profile is similar to the average TEC profile of 5 quietest days. By definition, GNSS TEC is the total number of electron integrated along in a 1 m^2 cross-sectional area along the transmission path from GNSS satellites to a receiver. Thus, the difference between the TEC profiles from ground-based GNSS observations and the TEC profile from Swarm satellite observations reflects the contribution of the ionosphere below the Swarm B altitude into the total electron content (~510 km). Figure 10 shows that at 03:33 UT (10:33 LT) on May 10, the difference between the GNSS TEC and Swarm TEC profiles was almost constant with latitude except at the EIA crest region, reflecting a fairly uniform ionosphere structure at this moment. On May 11, the geomagnetic storm was in its recovery phase. At 03:15 UT (10:33 LT), the GNSS TEC and Swarm TEC profiles show a significantly altered EIA structure compared to the quiet day, with crests moving approximately 5-6 degrees toward to the magnetic equator compared to May 10. The difference between the GNSS TEC and Swarm TEC profiles also changes, this difference in much greater at equatorial – low latitude. On May 12, The EIA structure has completely deteriorated, with the northern crest disappearing on both GNSS TEC and Swarm profiles. The difference between GNSS TEC and Swarm TEC profiles in the Southern Hemisphere is much greater than in the Northern one, demonstrating a clear hemispheric asymmetry of the ionosphere on this day. The hemispheric

asymmetry of the ionosphere on May 12 is also reflected in the difference between the GNSS TEC profile and the average quiet day GNSS TEC one at about 03:41 UT (10:31 LT). The time variation of the EIA shown on the GNSS TEC maps is also clearly reflected in the Swarm TEC profiles. The Swarm TEC at latitudes higher than 15°S on May 12 was higher than that observed on May 10, whereas in the Northern Hemisphere, TEC showed a depletion from around 10°N to beyond 30°N. Therefore, the two regions located at the outer edges of the EIA in the Northern and Southern Hemispheres, adjacent to the mid-latitude regions, responded in opposite directions. Under solstice conditions, the thermospheric winds generally blow from the summer hemisphere toward the winter hemisphere. However, during this storm, the thermospheric winds may have been more equatorward in the winter hemisphere, but this possibility requires further investigation. Ngwira et al. (2019) simulated the TIE-GCM winds for June 2015 storm which were equator-ward in both hemispheres. Therefore, these results should be further examined from the perspective of altitude variations at low latitudes in both the Northern and Southern Hemispheres, inferred from the vertical electron density profiles obtained from COSMIC observations.

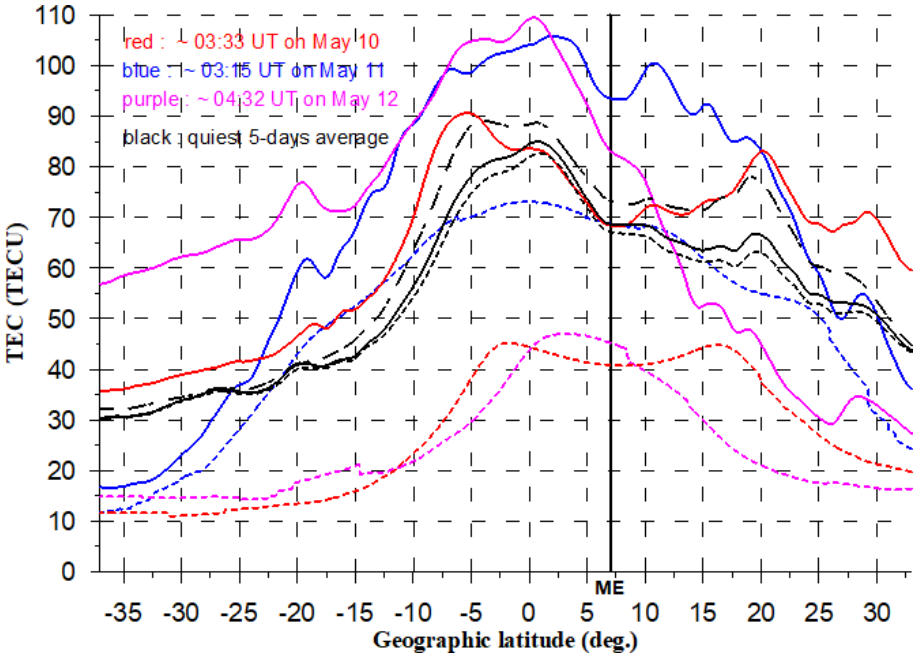


Figure 10. Display the GPS TEC (solid) and Swarm TEC (dash dash) at about 03:33 UT on 10 May (red), about 03:15 UT on May 11 (blue) and about 04:32 UT on May 12 (purple). The black lines represent the TEC profiles on the quietest 5-days average TEC map at about 03:33 UT (solid), 03:15 UT (dash-dash), and 04:31 UT (dot-dash). Magnetic equator (ME) is indicated at about 7°N (vertical bar).

3.6 The distribution of vertical electron density profiles derived from COSMIC data

The vertical electron density distribution estimated by the COSMIC/FORMOSAT-7 through radio occultation technique for the 90°E-120°E sectors is shown for the May 10 (blue) and May 12 (red and green) in Fig. 11 The left panel shows the low latitudes in the Northern Hemisphere and the right panel shows the low latitudes in Southern Hemisphere (in magnetic latitude).

On May 12, during the period from 00:00-02:00 UT, the F2 layer peak in the Northern Hemisphere was located at a lower altitude (about 207 km) compared to May 10 (about 325 km), while the vertical electron density profile decreased at all altitudes. In contrast, the southern EIA crest region, the F2 layer peak electron density was slightly higher than on the quiet day. The negative response trend in the Northern Hemisphere continued to intensify during the 03:00-05:00 UT period and persisted for the remainder of the day. During the 06:00-08:00 UT period (when the EIA is expected to be most developed), NmF2 values at low latitudes in the Northern Hemisphere were lower than those on the quiet day. Meanwhile, in the Southern Hemisphere, NmF2 at low latitudes was comparable to the quiet day, while at mid-latitudes it was higher than on the quiet day (Fig. 12). The increase in electron density observed

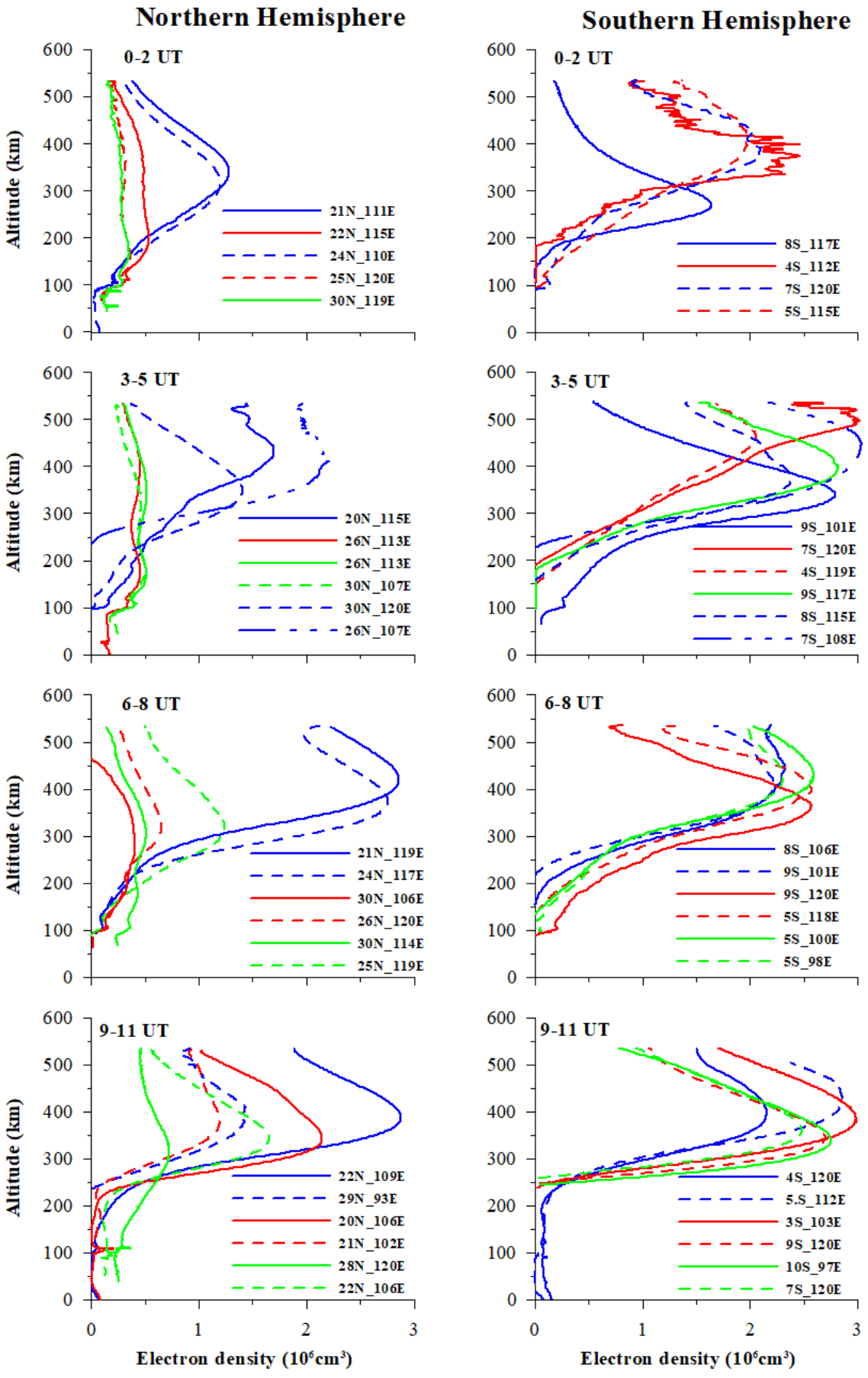


Figure 11. COSMIC-RO Ne profiles in the northern low latitude (left) and southern low latitude (right). Blue for May 10, red and green are profiles on May 12.

by COSMIC at mid-latitudes in the Southern Hemisphere was also seen in the TEC maps on this day (section 3.1). We highlight that consistently lower hmF_2 was recorded on the Northern Hemisphere as compared to the Southern Hemisphere. This can create an environment with a higher neutral density, thereby enhancing chemical recombination in the Northern Hemisphere. As a result, more severe plasma depletions were observed at northern low latitudes. Higher altitudes at low and mid-latitudes in the southern hemisphere help maintain electron density. As a result, electron density in the southern hemisphere remains stable, which also corresponds to less variation in the southern EIA crest amplitude.

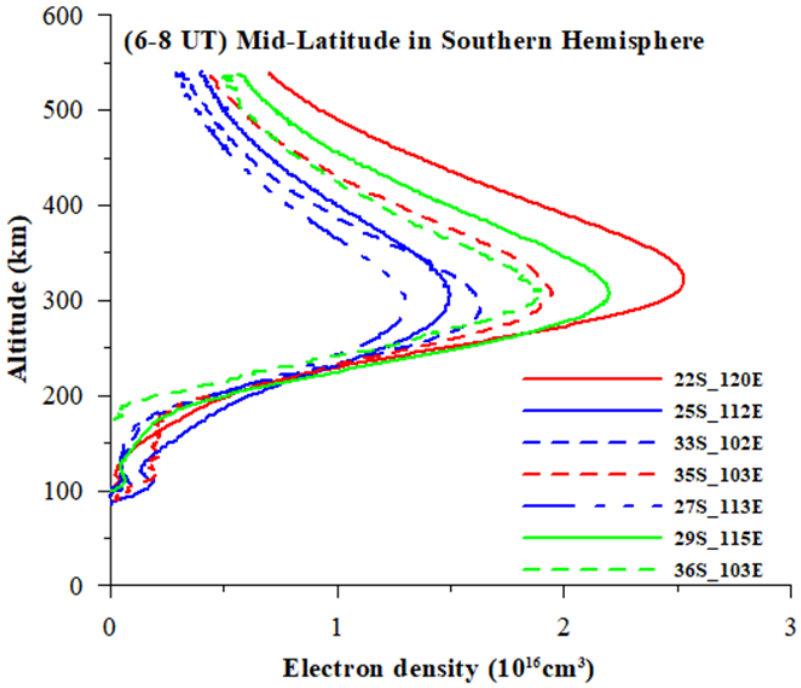


Figure 12. COSMIC-RO Ne profiles in the northern mid-latitude, blue profiles on May 10 and, red and green profiles on May 12.

3.7 Disturbance dynamo signature from the magnetic observatories

Using data from near-meridional chains of 13 magnetic stations (8 in Eastern Hemisphere, 5 in Western one), the global geomagnetic response to the May 10-11 magnetic storm has been studied by Chernogor et al. (2025). During geomagnetic storms, the PPEF represents the nearly prompt penetration of the magnetospheric convection electric field into low latitudes and is observed simultaneously at all longitudes during the main phase of the storm (Nishida, 1968). In contrast, D_{dyn} is associated with the DDEF (Le Huy and Amory-Mazaudier, 2005) and gives rise to anti-S_q oscillations, which are typically observed during the recovery phase of geomagnetic storms. In this paper, using the D_{dyn} calculation method (Younas et al., 2021) the ionospheric disturbance dynamo signature in magnetic field is estimated from the horizontal component of H for PHUT and GUAM observatories (Fig. 13). For PHUT (dip = 15.95°N), the strong disturbance dynamo signature D_{dyn} was estimate from 16:20 UT on May 11 to 11:40 UT on May 13. For GUAM (dip = 5.58°N), the D_{dyn} signature was seen from 15:30 UT on May 11 to 01:20 UT on May 13. The D_{dyn} effect at GUAM station is about 1 hour earlier than at PHUT station, possibly due to the difference in longitude between the two stations. The D_{dyn} effect at GUAM ends early on May 13, while the D_{dyn} effect at PHUT ends around midday on May 13, possibly because GUAM station is at a lower latitude than PHUT station. Therefore, the disturbance dynamo effect, commonly recognized as a dominant factor to equatorial-low latitude negative ionospheric storms, was identifiable in the magnetic variations only from the late evening to pre-midnight period (local time) on May 11. On the night of May 11, between 13:30 and 21:00 UT (Fig. 7), the hmF_2 height at the equator as well as at near the EIA crest was significantly enhanced. Note that the IMF B_z component shifted northward around 15:00 UT and stabilized around 0 during the later phases of the storm. During the uplift, hmF_2 at both the equator and the

near EIA crest exhibited a temporary decrease between ~15:30 and 18:00 UT. During this period, the DDEF became established, and the DDEF was eastward on the nighttime and contributed to the hmF_2 increase. On May 12, with the development of the DDEF, the TEC maps (Fig. 3) showed that the northern EIA nearly disappeared, while the southern EIA shifted equatorward. During the same period (00:00-12:00 UT), ionosonde observations showed that hmF_2 decreased and foF_2 increased at the magnetic equator, whereas foF_2 decreased sharply near the EIA crest.

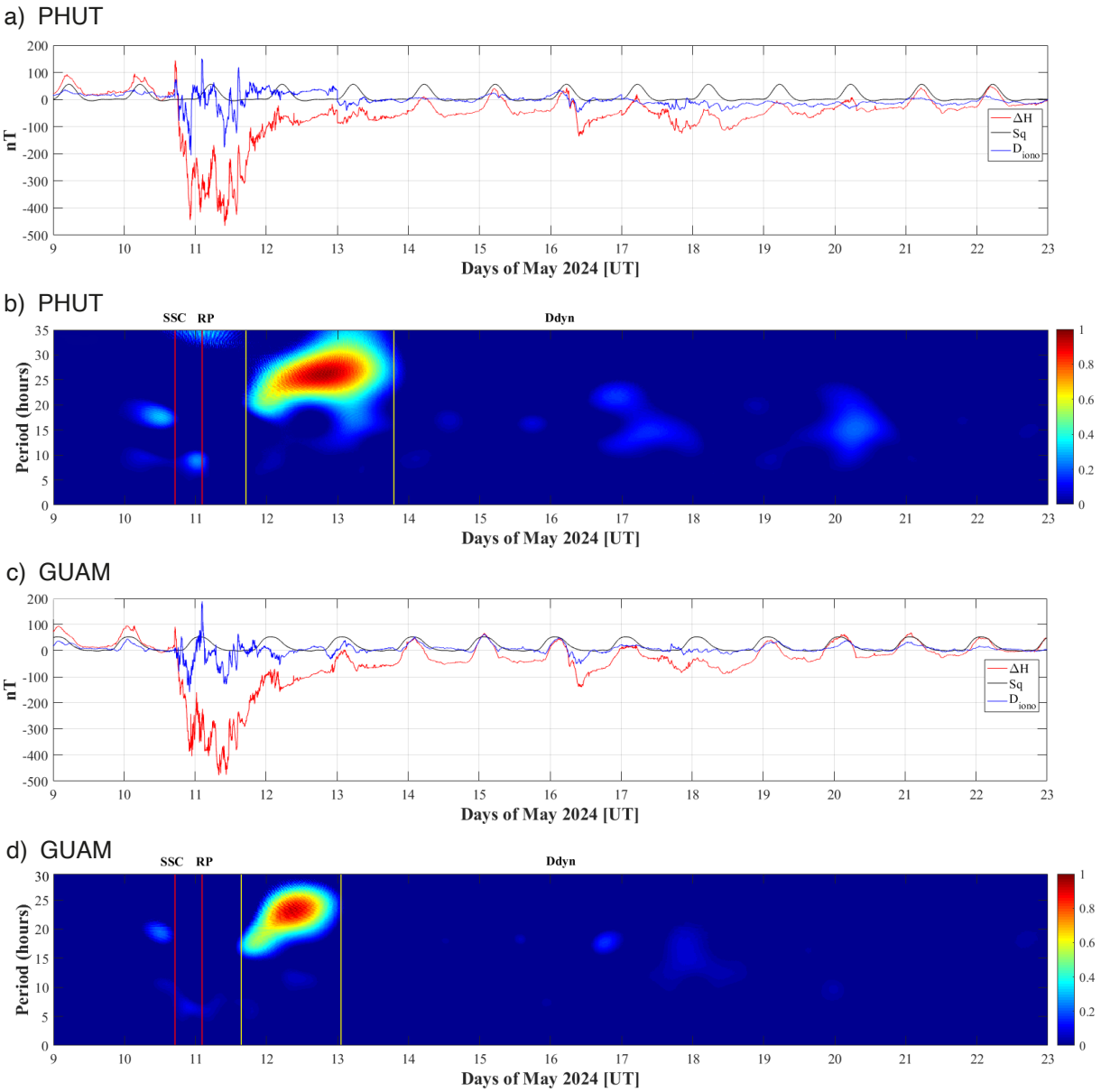


Figure 13. Magnetic variation at Phu Thuy (a) ΔH (red), S_q (black) and D_{iono} (blue); (b) D_{dyn} disturbance) and at GUAM observatories (c) ΔH (red), S_q (black) and D_{iono} (blue); (d) D_{dyn} disturbance) from May 09 to 22, 2024. The vertical yellow lines denote intervals where $D_{dyn} \geq 0.3$.

4. Discussion

4.1 Ionosphere response during the main phase

Decreases in hmF_2 and foF_2 in the Northern Hemisphere, as well as in TEC in both hemispheres, were observed during the main phase of the storm. The PPEF is eastward during daytime and westward during nighttime (Ambili et al., 2025).

In this case, since the storm commenced during nighttime, the electric field is expected to be westward. The in-phase superposition of the PPEF with the westward zonal electric field under nighttime conditions weakens the vertical $E \times B$ drift, thereby reducing the strength of the equatorial plasma fountain effect. Specifically, the plasma in the equatorial region is driven downward to lower altitudes with higher neutral density, leading to a reduction in plasma density due to enhanced recombination. During the May 2024 geomagnetic storm, a decrease in VTEC during the main phase was also observed over the Indian sector by Ambili et al. (2025). Thus, the decrease in foF_2 and TEC during the main phase can be attributed to the westward PPEF under nighttime conditions.

During the storm main phase, characterize by a negative vertical component of the interplanetary magnetic field ($B_z < 0$), the interactions between the solar wind and the southward B_z cause the eastward electric field to penetrate directly into the ionosphere (Nishida, 1968; Kikuchi et al., 2000; Fejer and Emmert, 2003). Typically, if the main phase occurs during the daytime, this PPEF can increase the crest amplitude of the EIA and pushes its position poleward (Lin et al., 2005; Le Huy et al., 2016, Pancheva et al., 2016). This behavior is also observed in the American longitude sector during the present storm (Aa et al., 2024; Tulasi Ram et al., 2024; Zhang et al., 2024; Astafyeva et al., 2025; Karan et al., 2024). In contrast, the main phase in the studied region from 17:05 UT on May 10 to 02:14 UT on May 11, corresponding to local nighttime (~00:05 LT on May 10) and morning hours (~09:14 LT on May 11). These local time conditions are associated with a weakened or underdeveloped EIA. Therefore, no pronounced daytime EIA response was observed during the main phase of the storm. This indicates that differences in the storm onset time and local time may result in different ionospheric responses.

4.2 Ionosphere response during the recovery phase

The ionosonde observations on May 11 (Fig. 6) showed that the repeated northward and southward reversals of the IMF B_z caused successively increases and decreases in hmF_2 and foF_2. Consequently, a rather interesting feature on this day is the temporal variation of foF_2, with up to four oscillations observed between 00:00 and 12:00 UT, due to the continuous reversals of the IMF B_z component. These oscillations contributed to the formation of a wave-like structure of the EIA (Fig. 3). This morphological pattern was also observed by Sun et al. (2024), Zhang et al. (2024), and Huang et al. (2025) over Asian-Australian sector. These studies indicated that the wave-like structures in the EIA and the multi-peak TEC oscillations are associated with TIDs. Although these features are likely associated with TIDs, a detailed investigation of TIDs is beyond the scope of the present study.

During the first day of the recovery phase (May 11), the amplitude of the northern EIA crest decreased, whereas that of the southern EIA crest remained nearly unchanged. Meanwhile, both EIA crests exhibited an equatorward shift. Compared with the quiet-day conditions, foF_2 increased slightly at the magnetic equator but decreased at the EIA crests. In the following, we discussed the possible physical mechanisms responsible for these observed features. When the IMF B_z is directed southward/northward, the PPEF generates eastward/westward electric fields, resulting in upward/downward fluctuations of the vertical plasma drift (Vz) (Fig. 14). Figure 14 shows the Vz estimated from hmF_2 at the BACL station for May 11-13, and the average Vz level on quiet days. In quiet-time conditions, Vz shows an upward trend during daytime, a downward trend at night, and a pre-reversal enhancement (PRE) around sunset. The upward drift enhanced electron density by moving the electron to higher altitude with lower recombination rates, while downward drift conversely reduced electron density. The vertical drift velocity Vz on day 11 shows multiple transitions between upward and downward states, suggesting the presence of alternate eastward and westward PPEFs, associated with several transitions of the IMF B_z component from southward to northward orientation. Thus, the IMF B_z component was unstable, undergoing continuous reversals over short timescales. As a result, the equatorial plasma fountain is suppressed, which limits the transport of plasma from equator to higher latitudes – an essential process for maintaining the EIA (Ambili et al., 2025).

During the intervals of eastward PPEF (00:00-03:59 UT and 06:00-11:00 UT), although hmF_2 increased significantly over the magnetic equator, foF_2 at the EIA crest decreased (Figs. 6 and 7). This suggests that the uplifted plasma was not efficiently transported from the magnetic equator to the EIA crests. This behavior may be attributed to the influence of a strong equatorward meridional wind. Poleward winds facilitate the transport of plasma from the equatorial region to low latitudes, thereby enhancing the diffusion along magnetic field lines. In contrast, equatorward winds tend to suppress this diffusion process, leading to markedly different ionospheric responses (Balan et al., 2013; Fuller-Rowell et al., 1994; Rishbeth, 1971). Strong equatorward meridional winds can inhibit the field-aligned diffusion of plasma toward low latitudes, leading to the formation of a local maximum near the equator (Ambili and

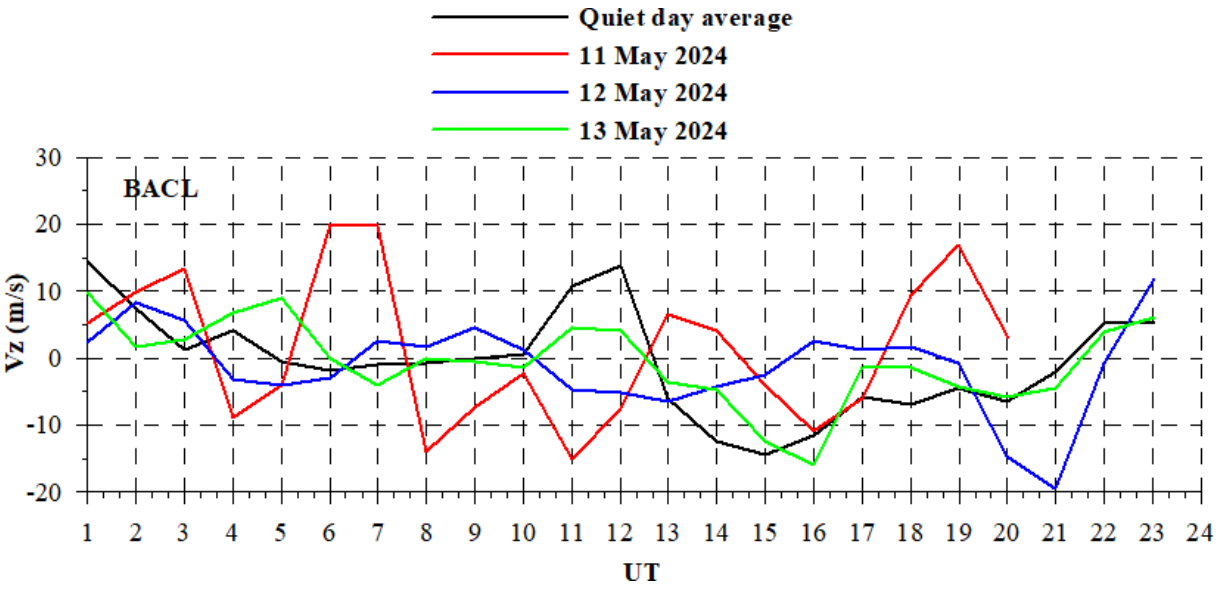


Figure 14. The vertical drift velocity (Vz) estimated from hmF_2 at the BACL station, the black line represents the quiet day average Vz, and the red, blue, and green lines represent V_z on May 11, 12, and 13, respectively. LT = UT+7.

Choudhary, 2022; Balan et al., 2009; Lin et al., 2005). Observations during the same storm by Ambili et al. (2025) and Jain et al. (2025) indicate that TEC increased at equatorial stations, while it decreased at stations near the EIA crests.

During the period from 07:10-08:50 UT, the hmF_2 increased substantially to values well above typical daytime levels (Fig. 6, exceeding 500 km). The foF_2 at BACL increased, whereas at PHUT it decreased markedly compared to the quiet-day values (Fig. 7). During this interval, the ionograms at the equator show the presence of an F3 layer (at virtual height around 800-900 km) above the F2 layer of the ionosphere (Fig. 8). The occurrence of the F3 layer is attributed 1) to the prompt penetration of intense convection electric fields, as in the case of superstorms (Lin et al., 2009), 2) to unusual equatorward winds that lift the plasma upward along magnetic field lines (Balan and Bailey, 1995; Sreeja et al., 2009, and references therein), or 3) to a combination of both mechanisms (Balan et al., 1998). A favorable combination of an eastward electric field and equatorward/eastward thermospheric winds can result in the formation of an F3 layer at dip-equator as a part of ascending F-layer of the ionosphere (Choudhary et al., 2023). The observed F3 layer, occurring simultaneously with the southward turning of the IMF B_z component and a significant increase in hmF_2, suggests the presence of PPEF. Since single-station ionosonde observations do not allow a quantitative separation of the relative contributions of electric fields and equatorward neutral winds during storm time, the observed F3 layer cannot be attributed solely to the effect of neutral winds. For this geomagnetic storm event, Evans et al. (2024) clearly demonstrated a thermospheric temperature difference of up to 400 K between high- and low-latitude regions using observations from the Global-scale Observations of the Limb and Disk (GOLD) mission to derive the $[O]/[N_2]$ ratio. This shows clearly indicating an equatorward wind activity on 11 May 2024. The existence of equatorward meridional winds has been confirmed by studies over Indian equatorial/low latitude region (Ambili et al., 2025; Ashok et al., 2025) and in the Asian region (Huang et al., 2025). The notable similarity between the simulation results and observations by Ashok et al. (2025) indicates that field-aligned plasma diffusion on May 11 was either negligible or very weak, suggesting the possible presence of the equatorward wind.

The negative ionospheric storm effect in the Northern Hemisphere on May 11 is believed to be due to changes in the neutral composition (e.g., Buonsanto, 1999; Mendillo, 2006, Spogli et al., 2024). A decrease in the $[O]/[N_2]$ ratio leads to an increase in the electron loss rate (Prölss, 1995) and produces a negative ionospheric storm effect (Prölss, 1995, de Abreu et al., 2023). Disturbance in neutral composition during magnetic storms are common in high-latitude region; however, under conditions of strong magnetic activity, such disturbances can extend from the auroral regions toward lower latitudes (Spogli et al., 2024).The previous results and discussions clearly demonstrate an enhancement of equatorward thermospheric winds. During magnetic storms, Joule heating in the high-latitude thermosphere leads to an upwelling of nitrogen-enriched air, which subsequently expands toward the equator, forming a composition bulge (Fuller-Rowell et al., 1994, 2002; Prölss, 1997). As the equatorward thermosphere winds propagate to the low-latitude and equatorial regions, cause a down-welling of the atmosphere, increasing the

column density of atomic oxygen. In the early phase of the wind surge, lighter atomic species such as O arrive earlier than heavier molecular species such as N_2 and O_2 (Ambili et al., 2025). Consequently, in the equatorial region, the increase in atomic oxygen enhances the $[O]/[N_2]$ ratio, leading to an increase of plasma density, and contributing to the positive ionospheric storm. In contrast, at the low latitude (EIA crest), the upward transport of molecular-rich air (N_2) reduces the $[O]/[N_2]$ ratio, resulting in decrease in plasma density, leading to negative storm phase in low latitudes. During this event, Evans et al. (2024) reported $[O]/[N_2]$ ratio decreases of up to 50% at mid-latitudes and increases of up to 50% at the equator in the American sector. Therefore, if the strong equatorward winds are sufficiently intense to reach the equatorial region, as observed along longitudes in the America (Evans et al., 2024), the composition disturbance $[O]/[N_2]$ can extend to EIA latitudes and cause a reduction in TEC amplitudes at the crests (Fuller-Rowell et al., 1994; Prölss, 1997).

Besides the disturbance composition effect (i.e., a reduced $[O]/[N_2]$ ratio), which contributes to negative ionospheric storm effects at low and middle latitudes, the DDEF also plays an important role (Blanc and Richmond, 1980). During the storm recovery phase, high-energy particles from the solar wind penetrate deeply into the polar atmosphere, heating it to create neutral winds that blow meridionally towards the equator. The complex interaction between the neutral winds and the magnetic field generates the ionospheric disturbance dynamo or DDEF (Blanc and Richmond, 1980). In this scenario the electric field in the equatorial region shifts westward, contrasting with the eastward electric field observed under normal conditions. This westward electric field induces a downward drift of the F-layer plasma, inhibits the transport of plasma from the equator to the low latitude, thereby weakening EIA, giving an apparent equatorward movement of EIA (Lin et al., 2005; Le Huy et al., 2016). However, in this study, the D_{dyn} (DDEF magnetic signature) was detected only around local midnight on May 11 (15-16 UT). This is in spite of the storm's main phase starting around 17:05 UT on May 10, and the recovery phase starting by 2:14 UT on 11 May. Thus, the role of the DDEF in producing the negative storm effect over the low- and mid-latitude regions on this day was negligible. Therefore, the observed ionospheric responses during the storm were likely controlled by the combined effects of PPEF, equatorward neutral winds, and storm-time variations in the $[O]/[N_2]$ composition ratio. Due to the lack of daytime neutral wind measurements and equatorial electric field observations, assessing the relative contributions of the PPEF, neutral winds, and compositional effects remain challenging. Future numerical simulations are needed to further clarify the relative importance of each of these factors.

The persistence of the PPEF during the recovery phase distinguished the ionospheric response on this day from that observed during other magnetic storms. For example, during the October-November 2003 storm (Lin et al., 2005), the March 2015 storm (Le Huy et al., 2016), and the December 2015 storm (Kalita et al., 2024), the combined effects of the DDEF and thermospheric $[O]/[N_2]$ depletion, in the absence of PPEF, resulted in the disappearance of one EIA crest.

On May 11, the hemisphere asymmetry of EIA was also observed. The amplitude of the northern EIA crest decreased compared to the pre-storm day, whereas the amplitude of the southern crest remained comparable to its pre-storm level; The northern EIA crest (~3°N magnetic latitude) shifted farther equatorward than the southern EIA crest (~6°S magnetic latitude). During a geomagnetic storm, a composition bulge form, characterized by an increase in the mean molecular mass. This composition bulge is transported by both the storm-induced and background wind fields. This geomagnetic storm occurred during the summer in the North Hemisphere and the winter in South Hemisphere, when the auroral region in the Northern Hemisphere received stronger solar EUV radiation than that in the Southern Hemisphere. As a result, the background thermospheric circulation in the Northern Hemisphere was directed equatorward, whereas in the Southern Hemisphere it was directed poleward. During the geomagnetic storm, disturbance neutral winds were directed equatorward in both hemispheres. In the Northern Hemisphere, the storm-time equatorward circulation was superimposed on the seasonal background circulation, which was also directed equatorward. This may have facilitated a more efficient transport of thermospheric composition disturbances toward lower latitudes. In contrast, in the Southern Hemisphere, the storm-induced equatorward circulation opposed the background poleward circulation, which may have inhibited the equatorward expansion of thermospheric composition disturbances from high to low latitudes (Fuller-Rowell et al., 1996; Yu et al., 2023). The seasonal difference between the summer and winter hemispheres contributed to the hemispheric asymmetry in the $[O]/[N_2]$ ratio (Fig. 9) over the equatorial and low-latitude regions (Fuller-Rowell et al., 1996). Zhang et al. (2024) studied detail magnetic storm May 2024 and shown that in Asian sector, the dayside TEC presented negative storm effects in the Northern Hemisphere and positive in the Southern Hemisphere, which may be related to the changes of the $[O]/[N_2]$ associated with the global circulation. Therefore, the summer-to-winter neutral wind circulation and the hemispheric asymmetry in the $[O]/[N_2]$ ratio may have been responsible for the hemispheric asymmetry in the EIA crest amplitude observed on May 11, 2024.

On May 12, a decrease in foF_2 was observed at PHUT, whereas foF_2 increased at BACL. At the same time, the northern EIA disappeared, while the southern EIA remained largely unaffected. On this day, although the $[O]/[N_2]$ ratio over the northern hemisphere study region showed signs of recovery (Fig. 9), TIMED/GUVI images indicated that the composition disturbance had extended to low latitudes over East Asia. This may imply the occurrence of equatorward meridional wind surges in the Northern Hemisphere during the storm, thereby limiting the transport of plasma from the equator to low latitudes. However, on this day, geomagnetic observations provided clear evidence for the presence of the DDEF. It is also worth noting that the IMF B_z turned northward at around 15:00 UT on May 11 and remained relatively stable around zero during the following days. Therefore, the PPEF was no longer expected to play a significant role in modulating the daytime EIA on May 12. The Vz during the period from 03:00-06:00 UT shows a downward trend, indicating a weakening of the fountain effect, and the EIA in the Northern Hemisphere was almost completely absent on this day. This observation provides evidence for the development of a westward disturbance dynamo electric field, which can suppress the formation of the EIA and subsequently produce a negative ionospheric response in the Northern Hemisphere. Therefore, the ionospheric response during the late recovery phase of the storm in the Northern Hemisphere was likely governed by the combined effects of the DDEF, neutral winds, and thermospheric $[O]/[N_2]$ variations.

A pronounced hemispheric asymmetry was also observed on this day, with a positive storm effect in the winter hemisphere (Southern Hemisphere) and a negative storm effect in the summer hemisphere (Northern Hemisphere). As discussed above, the negative storm effect is generally attributed to the combined effects of the DDEF and thermospheric $[O]/[N_2]$ depletion associated with composition disturbances. However, these electric field effects typically produce a symmetric response in both hemispheres, whereas we observed a markedly stronger response in the northern EIA, with the southern EIA region being almost unaffected. Therefore, the EIA suppression and the negative storm effects caused by DDEF must be modulated by other factors, such as neutral composition and meridional winds. It should be noted that the summer-winter asymmetry of neutral winds may also contribute to the hemispheric asymmetry of the EIA crests (Lin et al., 2005). As discussed above, Zhang et al. (2024) showed that the dayside TEC presented negative storm effects in the Northern Hemisphere and positive in the Southern Hemisphere, which may be related to the changes of the $[O]/[N_2]$ associated with the global circulation. However, they did not discuss the potential role of the DDEF on this day. Additionally, given the lack of $[O]/[N_2]$ observations in the Southern Hemisphere, it is difficult to attribute the observed hemispheric asymmetry to hemispheric differences in the $[O]/[N_2]$ ratio. Our analysis of the COSMIC vertical electron density profiles showed that hmF_2 at low and middle latitudes in the Southern Hemisphere was higher than that in the Northern Hemisphere. Therefore, the multi-instrument analysis presented in this study suggests that the TEC and EIA variations in the Southern Hemisphere were closely associated with changes in the F-region peak height and the redistribution of plasma within the ionosphere. The larger variation in altitude observed in the Southern Hemisphere compared to the Northern Hemisphere as shown by COSMIC vertical electron density profiles, as well as the increase/decrease of topside VTEC at the outer crest of the EIA in the Southern/Northern Hemisphere (Section 3.5), suggests the possible presence of transient equatorward neutral winds in the Southern Hemisphere. The equatorward winds can indirectly affect the density by raising the plasma along field lines to a greater altitude. The uplift to higher altitudes may allow the plasma to persist longer due to reduced chemical recombination rates, which could partly mitigate the negative ionospheric response associated with DDEF in the Southern Hemisphere. Conversely, the lower plasma altitude and stronger chemical recombination rates may promote a stronger negative ionospheric response in the Northern Hemisphere. However, since thermospheric wind observations are not available in the present study, this interpretation cannot be directly confirmed. Kalita et al. (2024) reported an interhemispheric asymmetry during the June 2015 geomagnetic storm and suggested the possible existence of transient equatorward winds in the Southern Hemisphere. Therefore, transient equatorward winds in the Southern Hemisphere may have partly modulated the DDEF effects over the study region and contributed to the interhemispheric asymmetry observed on May 12. However, the role of storm-time variations in the $[O]/[N_2]$ ratio should also be considered as a possible contributing factor.

On May 13, the northern EIA crest expanded poleward, while the TEC at the southern EIA crest increased significantly. According to Chernogor et al. (2025), this storm event was comprised of two storms. For the first storm Kpmax = 9, which was observed on May 10, 2024, and for the second storm, which occurred on the night of May 12-13, 2024, Kpmax = 6. This indicates that strong geomagnetic disturbances were recorded on May 13. On this day, the IMF B_z had stabilized, and the DDEF observed at the equatorial station (GUAM) lasted for only about one hour. At the same time, Vz shows a significant upward trend compared to the quiet day mean, which may enhance the fountain effect in the Northern Hemisphere, as evidenced by a poleward shift of the EIA crest relative

to the quiet day. Using GNSS data in Indian sector, Ambili et al. (2025) showed that VTEC peaks were recorded over Trivandrum and Bangalore, followed by subsequent peaks over Pune and Bhopal, indicating plasma diffusion from the equatorial region toward the crest locations. Chernogor and Bessarabova (2025) used F-region critical frequency data obtained from the international global ionospheric network GIRO [https://giro.uml.edu/index.html] (including stations in Europe and America) and reported a decrease in foF_2 in both the Eastern and Western Hemispheres on May 13. The discrepancy between these observations and our results further confirms that the ionospheric response to the geomagnetic storm varied with longitude.

Recently using the datasets from nine ground-based magnetometer stations, four ionosondes, and five GNSS stations in East Asia region (China and Japan) within the latitude range of 19.4°N-52.0°N, Xu et al. (2026) observed a negative ionospheric storm effect during the main phase and the recovery phase characterized by significant decreases in foF_2 and TEC. In the present study, our observations of the negative ionospheric storm effect are also consistent with the findings of Xu et al. (2026). They reported an increase in hmF_2 of approximately 400 km at the southernmost station, Guilin, during the main phase of the geomagnetic storm, with the magnitude of the increase gradually decreasing with latitude, while hmF_2 decreased by 100-200 km relative to the reference-day levels during the recovery phase. In contrast, our study shows that hmF_2 decreased at both the equatorial and low-latitude regions during the main phase. On the first day of the recovery phase (May 11), hmF_2 increased in both regions, whereas on May 12, hmF_2 decreased at the equator but remained relatively stable at low latitude. On both days, foF_2 increased at the equator but decreased at low latitude, accompanied by a weakening of the EIA structure, plasma accumulation near the equator, and a pronounced hemispheric asymmetry in the EIA structure. In addition, our study extends the analysis period through May 13. Xu et al. also identified DDEF from approximately 16:20 UT on May 11 to May 12, 2024, consistent with our findings. Although the two studies employed different methods to identify DDEF, their agreement provides independent supporting evidence for its presence during this period. Notably, Xu et al. reported a novel finding of quasi-periodic geomagnetic oscillations with periods of approximately 200 and 90 min attributed primarily to IMF B_z variations rather than TIDs. This finding differs from the TEC observations reported in our study and other cited studies.

5. Conclusions

In this paper, we present observational results from GPS-TEC, TEC from Swarm measurements, ionosonde data, TIMED/GUVI [O]/[N_2] ratio, vertical electron density profiles from COSMIC-2/FORMOSAT-7, and variations in the horizontal component of the magnetic field during the May 2024 magnetic storm. Utilizing multi-instruments data sources, we investigate the ionospheric response to this extreme space weather event over the East-Southeast Asia and Australia sector highlighting several interesting features. Our findings are summarized as follows:

- In the studied sector, the main phase of the storm entirely occurred on the night of May 10, 2024. Decrease of foF_2 and hmF_2 were observed at PHUT station near the crest region and BACL in the trough region of the EIA. In addition, TEC depletion was observed in both the EIA crest and equatorial regions of both hemispheres. These effects can be predominantly attributed to the westward PPEF during nighttime, which is associated with the strongly southward excursion of IMF B_z.
- During the recovery phase on May 11, the IMF B_z component exhibited complex fluctuations, repeatedly reversing from southward to northward, which caused strong variations in the PPEF. The presence of PPEF helps sustain the equatorial fountain effect, thereby maintaining well-defined EIA crests. However, its competition with equatorward meridional and transequatorial neutral winds during the storm leads to the formation of a double-crest structure and shifts the position of the EIA crests equatorward. During this period, multiple episodes of hmF_2 enhancement were observed, possibly associated with the eastward PPEF. The foF_2 increased in the equatorial region but decreased near the EIA crest. The equatorward displacement of the EIA crests implies an increase in TEC over the equatorial region and a decrease at low latitudes. In this case, the eastward PPEF failed to facilitate plasma diffusion from the equatorial region to low latitudes. The appearance of the F3 layer in the equatorial ionograms may indicate an equatorward wind surge, likely caused by auroral heating. This wind surge may have inhibited plasma diffusion from the dip equator while also contributing to changes in the thermosphere composition. The high-latitude composition bulge characterized by depleted [O]/[N_2] ratios was transported equatorward by neutral winds. As the composition bulge reached the equatorial region, downwelling may have increased the [O]/[N_2] ratio, thereby contributing to the further enhancement of foF_2 and TEC at the dip equator.

In contrast, at low latitudes, upwelling may have decreased the $[O]/[N_2]$ ratio, thereby contributing to the further reduction in foF_2 and TEC. Therefore, on May 11, the observed EIA structure and foF_2 variations can be attributed to the complex interactions among PPEF, neutral winds, and changes in the $[O]/[N_2]$ ratio. However, with the data used, it is difficult to accurately assess which of these mechanisms predominates. The hemispheric asymmetry of the EIA may be associated with hemispheric asymmetries in the $[O]/[N_2]$ ratio and neutral winds.

– On May 12, the second day of the recovery phase, the structure of the EIA became asymmetrical between the two hemispheres with the disappearance of the northern crest. On this day, the B_z almost stabilized around zero, and PPEF no longer played a significant role in the ionospheric variations. The D_{dyn} effect was clearly observed from PHUT and GUAM magnetic observatories, during the period from 15:30 UT on May 11 to 01:20 UT on May 13 for GUAM, and from 16:20 UT on May 11 to 11:40 UT on May 13 for PHUT, confirming the role of ionospheric disturbance dynamo during magnetic storm. The disappearance of the northern EIA crest can be explained by the combined effects of DDEF, meridional winds, and $[O]/[N_2]$ ratio variation. The hemispheric asymmetry of the EIA, together with the TEC enhancement at southern mid-latitudes, may be associated with a transient equatorward neutral wind in the Southern Hemisphere. However, the role of storm-time variations in the $[O]/[N_2]$ ratio should also be considered as a possible contributing factor.
– An unusual enhancement of the southern EIA amplitude and a poleward extension of both crests were observed on 13 May. These observations may suggest an enhanced equatorial fountain effect on that day. However, the mechanisms leading to larger drifts in the post-storm period are still unclear. Further investigations are required to understand the physical processes responsible for this enhancement.
– The observations presented in this paper demonstrate the complex interactions in the magnetosphere-thermosphere-ionosphere system during storms could be served as a foundation for modeling studies of ionospheric responses during storms.

Data and sharing resources. Ionosonde data at BACL can be downloaded at https://wdc.nict.go.jp/Ionosphere/archive/ionog_viewer_fmcw_ms/. Ionosonde data at PHUT can be obtained by sending a request to vp@ies.vast.vn. The Earth's magnetic field data at PHUT and GUAM geomagnetic observatories are available on the websites http://www.obsmag.info and http://www.intermagnet.org, respectively. Data of Vx, IMF B_z are obtained from the ACE Science Center http://izw1.caltech.edu/ACE/ASC/level2/lvl2DATA_SWEPAM.html. The SYM-H index available at World Data Center for Geomagnetism, Kyoto, Japan (https://wdc.kugi.kyoto-u.ac.jp/dst_realtime/index.html), and Kp geomagnetic activity index at https://kp.gfz-potsdam.de/en/. TIMED-GUVI $[O]/[N_2]$ data are available on the https://spdf.gsfc.nasa.gov/pub/data/timed/guvi/. Swarm data are provided by the European Space Agency (ESA) at https://swarm-diss.eo.esa.int/. The COSMIC-2 raw data are available in the COSMIC Data Analysis and Archive Center (CDAAC) at Index of/gnss-ro/cosmic2/provisional/spaceWeather/level2/.

Acknowledgments. Vietnam Academy of Science and Technology funds this research under grant VAST05.06/25-26. The ionosonde data at Bac Lieu are available on the website https://wdc.nict.go.jp/Ionosphere/archive/ionog_viewer_fmcw_ms/. The GNSS data are available on the websites https://cddis.nasa.gov/archieve/gnss/data/daily/ and http://ga-gnss-data-rinex-v1.s3.anmazonaws.com/index.html#public/daily/. Thanks the NAVIS center, SOICT, for providing the HUS2 station data. The GPS data of IES stations are on the database of the Institute of Earth Sciences, VAST (https://ies.vast.vn). The Swarms data are available at https://swarm-diss.eo.esa.int/. The software to create the plots: Generic Mapping Tools (GMT) http://www.generic-mapping-tools.org.

References

Aa, E., Y. Chen and B. Luo (2024). Dynamic expansion and merging of the equatorial ionization anomaly during the 10-11 May 2024 super geomagnetic storm, Remote Sens., 16, 22, 4290, doi:10.3390/rs16224290.

Ambili, K. M. and R. K. Choudhary (2022). On the impact of meridional wind circulation changes in the electron density distribution over the Indian equatorial and low latitude ionospheric region during a severe geomagnetic storm, Adv. Space Res., 70, 7, 2058-2069, doi:10.1016/j.asr.2022.06.027.

Ambili, K. M., R. K. Choudhary, A. Ashok, A. Potdar et al. (2025). The impact of 11 May 2024 great geomagnetic storm on the plasma distribution over the Indian equatorial/low latitude ionospheric region, J. Geophys. Res. Space Phys., 130, 4, e2024JA033368, doi:10.1029/2024JA033368.

Appleton, E. (1946). Two anomalies in the ionosphere, Nature, 157, 691.

Ashok, A., K. M. Ambili, R. K. Choudhary and G. Lu (2025). Unique signatures of meridional wind variations on the electron density distribution over the dip equator, Geophys. Res. Lett., 52, 18, e2025GL117926, doi:10.1029/2025GL117926.

Astafyeva, E., B. Maletckii, M. Förster, I. D. Ouar et al. (2025). Electrodynamic and ionospheric puzzles of the 10-11 May 2024 geomagnetic superstorm, J. Geophys. Res. Space Phys., 130, e2024JA033284, doi:10.1029/2024JA033284.

Balan, N. and G. J. Bailey (1995). Equatorial plasma fountain and its effects: Possibility of an additional layer, J. Geophys. Res. Space Phys., 100, A11, 21421-21432, doi:10.1029/95JA01555.

Balan, N., I. S. Batista, M. A. Abdu, J. MacDougall et al. (1998). Physical mechanism and statistics of occurrence of an additional layer in the equatorial ionosphere, J. Geophys. Res. Space Phys., 103, A12, 29169-29181, doi:10.1029/98JA02823.

Balan, N., J. Souza and G. Bailey (2018). Recent developments in the understanding of equatorial ionization anomaly: A review, J. Atmos. Sol. Terr. Phys., 171, 3-11, doi:10.1016/J.JASTP.2017.06.020.

Balan, N., K. Shiokawa, Y. Otsuka, S. Watanabe et al. (2009). Super plasma fountain and equatorial ionization anomaly during penetration electric field, J. Geophys. Res., 114, A3, A03310, doi:10.1029/2008ja013768.

Balan, N., Y. Otsuka, M. Nishioka, J. Liu et al. (2013). Physical mechanisms of the ionospheric storms at equatorial and higher latitudes during the recovery phase of geomagnetic storms, J. Geophys. Res. Space Phys., 118, 5, 2660-2669, doi:10.1002/jgra.50275.

Blanc, M. and A. D. Richmond (1980). The ionospheric disturbance dynamo, J. Geophys. Res., 85, A4, 1669-1686, doi:10.1029/JA085iA04p01669.

Buonsanto, M. (1999). Ionospheric storms-a review, Space Sci. Rev., 88, 3, 563-601, doi:10.1023/A:1005107532631.

Burns, A. G., T. L. Killen and R. G. Roble (1991). A theoretical study of thermospheric composition perturbations during an impulsive geomagnetic storm, J. Geophys. Res, 96, 14, 153-167, doi:10.1029/91JA00678.

Carter, B. A., R. Pradipta, T. Dao, J. L. Currie et al. (2023). The ionospheric effects of the 2022 Hunga Tonga Volcano eruption and the associated impacts on GPS Precise Point Positioning across the Australian region, Space Weather, 21, e2023SW003476, doi:10.1029/2023SW003476.

Chernogor, L. F. (2025a). What are a geospace storm and a pan-planetary storm, Avd. Space Res., 76, 5640-5657, doi:10.1016/j.asr.2025.08.016.

Chernogor, L. F. (2025b). Energetics of physical processes operated on May 8-12, 2024: from the solar storm to lithospheric disturbances, Adv. Space Res., 75, 4825-4849, doi:10.1016/j.asr.2024.12.069.

Chernogor, L. F. and V. O. Bessarabova (2025). Global manifestations of a unique geospace storm on May 10-13, 2024, in the F region of the ionosphere, Kinematic and Physics of Celestial bodies, 41, 209-220, doi:10.3103/S0884591325050022.

Chernogor, L. F., V. T. Rozumenko, M. B. Shevelev, J. Wang et al. (2025). Global geomagnetic response to the extreme geospacestorm of May 10-11, 2024, Adv. Space Res., 76, 939-967, doi:10.1016/j.asr.2025.05.004.

Choudhary, M., B. R. Kalita, B. Rai, D. Chakrabarty et al. (2025). Hemispherically and longitudinally asymmetric ionospheric response to the 23-24 March 2023 geomagnetic disturbances at three pairs of conjugate stations, J. Geophys. Res. Space Phys., 130, e2024JA033520, doi:10.1029/2024JA033520.

Choudhary, R. K., J. P. St. Maurice and K. M. Ambili (2023). The particularly clean response of the Indian sector to a strong but short lived geomagnetic storm, Adv. Space Res., 73, 3693-3707, doi:10.1029/2024JA033368.

Cooper, G. R. J. and D. R. Cowan (2008). Comparing time series using wavelet-based semblance analysis, Computers & Geosciences, 34, 2, 95-102, doi:10.1016/j.cageo.2007.03.009.

de Abreu, A. J., E. Correia, R. de Jesus, K. Venkatesh et al. (2023). Statistical analysis on the ionospheric response over South American mid- and near high-latitudes during 70 intense geomagnetic storms occurred in the period of two decades, J. Atmos. Sol. Terr. Phys., 245, 106060, doi:10.1016/j.jastp.2023.106060.

Evans, J. S., J. Correira, J. D. Lumpe, R. W. Eastes et al. (2024). Gold observations of the thermospheric response to the 10-12 May 2024 Gannonsuperstorm, Geophys. Res. Lett., 51, 16, e2024GL110506, doi:10.1029/2024gl110506.

Fejer, B. G. and L. Scherliess (1995). Time dependent response of equatorial ionospheric electric fields to magnetospheric disturbances, Geophys. Res. Lett., 22, 851-854, doi:10.1029/95GL00390.

Fejer, B. G. and J. T. Emmert (2003). Low latitude ionospheric disturbance electric field effects during the recovery phase of the 19-21 October 1998 magnetic storm, J. Geophys. Res., 108, A12, 1454, doi:10.1029/2003JA010190.

Fejer, B. G., C. A. Gonzales, D. T. Farley, M. C. Kelley et al. (1979). Equatorial electric field during magnetically disturbed conditions: 1. the effect of interplanetary magnetic field, J. Geophys. Res, 84, 5797, doi:10.1029/JA084iA10p05797.

Fejer, B. G., R. W. Spiro, R. A. Wolf and J. C. Foster (1990). Latitudinal variation of perturbation electric fields during magnetically disturbed periods: 1986 SUNDIAL observations and model results, Ann. Geophysicae, 8, 441-454.

Friis-Christensen, E., H. Lühr, D. Knudsen and R. Haagmans (2008). Swarm – An Earth Observations Mission investigating Geospace, Adv. Space Res., 41, 210-216, doi:10.1016/j.asr.2006.10.008.

Fuller-Rowell, T. J., M. V. Codrescu, R. G. Roble and A. D. Richmond (1998). How does the thermosphere and ionosphere react to a geomagnetic storm?, in Magnetic Storms, B. T. Tsurutani, W. D. Gonzalez, Y. Kamide and J. K. Arballo (Editors), Geophys, Monogr. Ser., 98, 203-225, doi:10.1029/gm098p0203.

Fuller-Rowell, T. J., M. V. Codrescu, R. J. Moffett and S. Quegan (1994). Response of the thermosphere and ionosphere to geomagnetic storms, J. Geophys. Res., 99, A3, 3893-3914, doi:10.1029/93JA02015.

Fuller-Rowell, T. M., G. H. Millward, A. D. Richmond and M. V. Codrescu (2002). Storm-time changes in the upper atmosphere at low latitudes, J. Atmos. Sol. Terr. Phys., 64, 1383, doi:10.1016/S1364-6826(02)00101-3.

Fuller-Rowell, T. J., M. V. Codrescu, R. J. Moffett and S. Quegan (1996). On the Seasonal Response of the Thermosphere and Ionosphere to Geomagnetic Storms, J. Geophys. Res., 101, 2343-2353, doi:10.1029/95JA01614.

Ghosh, S. (2024). Sky Gazers Capture Rare Red Aurora from Himalayan Observatory, Nature India, doi:10.1038/d44151-024-00068-w.

Greshko, M. (2024). Extreme Solar Storm Generated Aurorae and 'Surprise', Science, doi:10.1126/science.zoakd5z.

Guo, X., B. Zhao, T. Yu, H. Hao et al. (2024). East-west difference in the ionospheric response during the recovery phase of May 2024 super geomagnetic storm over the East Asian, J. Geophys. Res. Space Phys., 129, e2024JA033170, doi:10.1029/2024JA033170.

Huang, F., J. Lei, X. Yue, Z. Li et al. (2025). Interplay of gravity waves and disturbance electric fields to the abnormal ionospheric variations during the 11 May 2024 superstorm, AGU Advances., 6, e2024AV001379, doi:10.1029/2024AV001379.

Jain, A., R. Trivedi, S. Jain and R. K. Choudhary (2025). Effects of the Super Intense Geomagnetic Storm on 10-11 May, 2024 on Total Electron Content at Bhopal, Adv. Space Res., 75, 1, 953-965, doi:10.1016/j.asr.2024.09.029.

Kalita, B. R., P. K. Bhuyan, M. Choudhary, D. Chakrabarty et al. (2024). The differential conjugate hemisphere ionospheric response during solstice storms and the winter side maxima, Adv. Space. Res., 73, 1893-1907, doi:10.1016/j.asr.2023.11.025.

Karan, D. K., C. R. Martinis, R. E. Daniell, R. W. Eastes et al. (2024). GOLD observations of the merging of the Southern Crest of the equatorial ionization anomaly and aurora during the 10 and 11 May 2024 Mother's Day super geomagnetic storm, Geophys. Res. Lett., 51, e2024GL110632, doi:10.1029/2024GL110632.

Kelley, M. C., J. J. Makela, J. L. Chau and M. J. Nicolls (2003). Penetration of the solar wind electric field into the magnetosphere/ionosphere system, Geophys. Res. Lett., 30, 4, 1158, doi:10.1029/2002GL016321.

Kikuchi, T., H. Lühr, K. Schlegel, H. Tachihara et al. (2000). Penetration of auroral electric fields to the equator during a substorm, J. Geophys. Res., 105, 23251-23261, doi:10.1029/2000JA900016.

Klobuchar, J (1986). Design and characteristics of the GPS ionospheric time-delay algorithm for single frequency users, in Proceedings of PLAN'86 Position Location and Navigation symposium, Las Vegas, Nevada, 280-286.

Krisman, L. G., T. K. Pant, T. Manu, C. Vineeth et al. (2025). Indian equatorial ionosphere under the influence of the May 2024 geomagnetic storm: Insights into electric field, plasma irregularities and F-region dynamics, Earth Space Sci., 12, 5, e2024EA004116, doi:10.1029/2024EA004116.

Le Huy, M. and C. Amory-Mazaudier (2005). Magnetic signature of the ionospheric disturbance dynamo at equatorial latitudes: "D_{dyn}", J. Geophys. Res., Space Physics, 110, A10, doi:10.1029/2004JA010578.

Le Huy, M., C. Amory-Mazaudier, R. Fleury, A. Bourdillon et al. (2014). Time variations of the total electron content in the Southeast Asian equatorial ionization anomaly for the period 2006-2011, Adv. Space Res., 54, 355-368, doi:10.1016/j.asr.2013.08.003.

Le Huy, M., L. Tran Thi, R. Fleury, C. Amory Mazaudier et al. (2016). TEC variations and ionospheric disturbances during the magnetic storm in March 2015 observed from continuous GPS data in the Southeast Asia region, Vietnam J. Earth Sci., 38, 3, 287-305, doi:10.15625/0866-7187/38/3/8714.

Lin, C. H., A. D. Richmond, J. Y. Liu, G. J. Bailey et al. (2009). Theoretical study of new plasma structures in the low-latitude ionosphere during a major magnetic storm, J. Geophys. Res. Space Phys., 114, A05303, doi:10.1029/2008JA013951.

Lin, C. H., A. D. Richmond, J. Y. Liu, H. C. Yeh et al. (2005). Large-scale variations of the low-latitude ionosphere during the October November 2003 superstorm: Observational results, J. Geophys. Res., 110, A09S28, doi:10.1029/2004JA010900.

Lu, G., A. D. Richmond, B. A. Emery and R. G. Roble (1995). Magnetosphere-ionosphere-thermosphere coupling: Effect of neutral winds on energy transfer and field-aligned current, J. Geophys. Res., 100, A10, 19, 643-659, doi:10.1029/95JA00766.

Mannucci, A., B. T. Tsurutani, B. A. Iijima, A. Komjathy et al. (2005). Dayside global ionospheric response to the major interplanetary events of October 29-30, 2003 Halloween storms, Geophys. Res. Lett., 32, 12, doi:10.1029/2004GL021467.

Mendillo, M. (2006). Storms in the ionosphere: Patterns and processes for total electron content, Rev. Geophys., 44, 4, doi:10.1029/2005RG000193.

Namba, S. and K. I. Maeda (1939). Radio wave propagation, Corona Publishing, Tokyo, 86.

Ngwira, C. M., J. B. Habarulema, E. Astafyeva, E. Yizengaw et al. (2019). Dynamic Response of Ionospheric Plasma Density to the Geomagnetic Storm of 22-23 June 2015, J. Geophys. Res., Space Phys., 124, 8, doi:10.1029/2018JA026172.

Nishida, A. (1968). Geomagnetic D_p2 fluctuations and associated magnetospheric phenomena, J. Geophys. Res., 73, 5, 1795-1803, doi:10.1029/JA073i005p01795.

Oyekola, O. S., A. Ojo, J. Akinrimisi and E. R. dePaula (2007). Seasonal and solar cycle variability in F-region vertical plasma drifts over Ouagadougou, J. Geophys. Res., 112, A12306, doi:10.1029/2007JA012560.

Pancheva, D., P. Mukhtarov and B. Andonov (2016). Global structure of ionospheric TEC anomalies driven by geomagnetic storms, J. Atmos. Sol. Terr. Phys., 145, 170-182, doi:10.1016/j.jastp.2016.04.015.

Prölss, G. W. (1997). Magnetic storm associated perturbations of the upper atmosphere, in Magnetic storms, Geophys. Monogr. Ser., 98, 227-241, doi:10.1029/GM098p0227.

Prölss, G. W. (1995). Ionospheric F-region storms, in Handbook of Atmospheric Electrodynamics, H. Volland (Editor), CRC Press, Boca Raton, FL, USA, 195-248.

Richmond, A. D., C. Peymirat and R. G. Roble (2003). Long lasting disturbances in the equatorial ionospheric electric field simulated with a coupled magnetosphere-ionosphere thermosphere model, J. Geophys. Res., 108, A3, 1118, doi:10.1029/2002JA009758.

Rishbeth, H. (1971). The F-layer dynamo, Planet, Space Sci., 19, 2, 263-267, doi:10.1016/0032-0633(71)90205-4.

Rishbeth, H., T. J. Fuller-Rowell and A. D. Rodger (1987). F-layer storms and thermospheric composition, Phys. Scr., 36, 327-336, doi:10.1088/0031-8949/36/2/024.

Seba, E. B., M. Nigussie and M. B. Moldwin (2018). The relationship between equatorial ionization anomaly and nighttime equatorial spread F in East Africa, Adv. Space Res., 62, 7, 1737-1752.

Spogli, L., T. Alberti, P. Bagiacchi, L. Cafarella et al. (2024). The effects of the May 2024 Mother's Day superstorm over the Mediterranean sector: from data to public communication, Ann. Geophys., 67, 2, PA218, doi:10.4401/ag-9117.

Sreeja, V., C. Vineeth, T. K. Pant, S. Ravindran et al. (2009). Role of gravity wavelike seed perturbations on the triggering of ESF: A case study from unique dayglow observations, Ann. Geophysicae, 27, 313-318, doi:10.5194/angeo-27-313-2009.

Sun, W., G. Li, S. R. Zhang, B. Zhao et al. (2024). Complex ionospheric fluctuations over East and Southeast Asia during the May 2024 super geomagnetic storm, J. Geophys. Res. Space Phys., 129, e2024JA033096, doi:10.1029/2024JA033096.

Titheridge, J. (1985). Ionogram analysis with the generalized program POLAN, World Data Center Report, UAG-93, WDC-A-STP, Boulder, CO, 194.

Torrence, C. and P. G. Compo (1998). A Practical Guide to Wavelet Analysis, Bull. Amer. Meteor. Soc., 79, 1, 61-78, doi:10.1175/1520-0477(1998)079<0061:apgtwa>2.0.co;2.

Tsurutani, B. T., O. P. Verkhoglyadova, A. J. Mannucci, A. Saito et al. (2008). Prompt penetration electric fields (PPEFs) and their ionospheric effects during the great magnetic storm of 30-31 October 2003, J. Geophys. Res. Space Phys., 113, A12, 5311, doi:10.1029/2007JA012879.

Tulasi Ram, S., B. Veenadhari, A. P. Dimri, J. Bulusu et al. (2024). Super-intense geomagnetic storm on 10-11 May 2024: Possible mechanisms and impacts, Space Weather, 22, 12, e2024SW004126, doi:10.1029/2024SW004126.

Xu, T., Y. Liu, L. Chernogor, Z. Jin et al. (2026). Multi-instrument observations of the geospace storm features over China region during May 10-12, 2024, J. Atmos. Solar Terr. Phys., 284, doi:10.1016/j.jastp.2026.106843.

Younas, W., C. Amory-Mazaudier, M. Khan and M. Le Huy (2021). Magnetic signatures of ionospheric disturbance dynamo for CME and HSSWs generated storms, Space Weather, 19, e2021SW002825, doi:10.1029/2021SW002825.

Yu, T., X. Cai, Z. Ren, Z. Wang et al. (2023). Investigation of interhemispheric asymmetry of the thermospheric composition observed by GOLD during the first strong geomagnetic storm in solar-cycle 25, 1: IMF By effects, J. Geophys. Res., Space Physics, 128, e2023JA031429, doi:10.1029/2023JA031429.

Zhang, R., L. Liu, Y. Yang, W. Li et al. (2024). Ionosphere responses over Asia-Australian and American sectors to the 10-12 May 2024superstorm, J. Geophys. Res. Space Phys., 129, e2024JA033071, doi:10.1029/2024JA033071.

Zhao, B., W. Wan, L. Liu and Z. Ren (2009). Characteristices of the ionospheric total electron content of the equatorial ionization anomaly in the Asian-Australian region during 1996-2004, Ann. Geophysicae, 27, 3861-3873.

*** CORRESPONDING AUTHOR: Minh LE HUY**,
Institute of Earth Sciences, Vietnam Academy of Science and Technology, Hanoi, Vietnam
e-mail: lhminhigp@gmail.com

© 2026 the Author(s).
Open Access. This article is licensed under a Creative Commons Attribution 4.0 International License